- 1 Comparing paleo-oxygenation proxies (benthic foraminiferal surface porosity, I/Ca,
- 2 authigenic uranium) on modern sediments and the glacial Arabian Sea

Wanyi Lu<sup>1\*</sup>, Yi Wang<sup>1</sup>, Delia W. Oppo<sup>1</sup>, Sune G. Nielsen<sup>1</sup>, Kassandra M. Costa<sup>1</sup>

5

Department of Geology and Geophysics, Woods Hole Oceanographic Institution, Woods Hole, MA,
 USA

8

\*Correspondence to W. Lu: wlu@whoi.edu

11

12

13

14

15

16

17

18

19

20

21

22

23

24

25

26

27

#### Abstract

Oceanic oxygen reconstructions of the last glacial period are needed to understand the mechanisms of glacial deep ocean carbon storage and to validate climate model simulations. However, existing bottom-water oxygen (BWO) reconstructions are ambiguous due to limitations of each paleo-BWO proxy. Here we present data from three proxies for BWO: benthic foraminiferal surface porosity, benthic foraminiferal iodine/calcium (I/Ca), and authigenic uranium (aU), from globally distributed core-top samples, and we evaluate the potential advantages and limitations of these BWO proxies on global and regional scales. All three proxies are most sensitive to changes at relatively low BWO concentrations (< 50 µmol/kg). Benthic foraminiferal surface porosity shows a global correlation with BWO between 0 and 100 µmol/kg and is predominantly controlled directly by BWO rather than other potential functionalities of surface cores such as organic carbon uptake and respiratory CO<sub>2</sub> release. Low benthic I/Ca can identify low BWO (< 50 μmol/kg), whereas higher benthic I/Ca are not associated with specific BWO, possibly due to additional dependence of I/Ca on temperature, salinity, carbonate ion concentration, or water mass mixing at higher BWO. The relationship between aU and BWO is regionally dependent. In the Arabian Sea, variable aU enrichments occur only within the Oxygen Minimum Zone (OMZ), driven by high export production and organic matter fluxes to the sediment. Finally, we combine for aminiferal surface porosity, I/Ca and aU to generate the first quantitative glacial-Holocene BWO reconstructions using a sediment core taken from within the modern Arabian Sea OMZ. All three proxies consistently suggest BWO < 50  $\mu$ mol/kg in the shallow Arabian Sea during the last ~30 kyr, with relatively higher BWO during the glacial period than the Holocene. Our study provides new insights on merits and limitations on these BWO proxies and confirms the importance of multi-proxy reconstructions for more reliable paleo-BWO estimates.

## Keywords

- 38 Bottom-water oxygen, benthic foraminifera, benthic surface porosity, iodine/calcium,
- 39 authigenic uranium, Arabian Sea

# **Key points**

- Benthic foraminiferal surface porosity, I/Ca, and authigenic uranium are most sensitive
   to low BWO concentrations.
- Multi-proxy reconstructions in the modern Arabian Sea OMZ show consistently BWO
- $< 50 \mu mol/kg$  during the last 30 kyr.
  - Glacial BWO in the Arabian Sea OMZ may have been 10-15 μmol/kg higher than the Holocene.

#### 1. Introduction

Dissolved oxygen in the oceans is a key parameter in the global carbon cycle with impacts on ocean biogeochemistry and marine ecosystems. Reconstructions of bottom water oxygen (BWO) concentrations for the last glacial period and deglaciation advance our understanding how BWO responds to climate changes. With recent developments of semi-quantitative paleo-BWO proxies, glacial BWO reconstructions have been used to: (1) quantify glacial ocean carbon storage utilizing the Redfield ratios of respiratory CO<sub>2</sub> and consumption of oxygen (Hoogakker et al., 2015, 2018; Anderson et al., 2019); (2) compare with global climate model output to understand the driving mechanisms of glacial oxygenation changes (Yamamoto et al., 2019; Cliff et al., 2021; Kobayashi et al., 2021).

The glacial climate model predictions, however, show considerable mismatch with BWO

The glacial climate model predictions, however, show considerable mismatch with BWO reconstructions in some regions (i.e., northern Indian Ocean and northern Pacific Ocean) (Yamamoto et al., 2019; Cliff et al., 2021). This may be in part because estimates of BWO in glacial oceans are uncertain due to biases and limitations in each paleo-BWO proxy. Table 1 summarizes five recently-developed semi-quantitative BWO proxies, which provide an estimated oxygen concentration, in contrast to qualitative proxies (e.g., bulk sedimentary  $\delta^{15}$ N, laminations, and redox-sensitive trace metals) (Jaccard and Galbraith, 2012; Moffit et al., 2015). All the semi-quantitative proxies have been calibrated using recent or core-top samples, on global or regional scales. These BWO proxies can be broadly divided into two groups: (1) biological proxies: benthic foraminiferal surface porosity (i.e., surface area percentages covered by pores) (Rathburn et al., 2018; Tetard et al., 2021a); benthic foraminiferal distributions and morphologies (i.e., average size and roundness) (Erdem et al., 2020; Tetard et al., 2021a, b), and (2) geochemical proxies: the carbon isotope gradient between epifaunal

benthic foraminifera (living on top of sediments) Cibicidoides wuellerstorfi and deep infaunal benthic foraminifera (living in the sediments) Globobulimina spp. ( $\Delta\delta^{13}$ C) (McCorkle and Emerson, 1988; Hoogakker et al., 2015); preservation of C<sub>37</sub> alkenone in the sediments (Anderson et al., 2019); and benthic I/Ca (Glock et al., 2014; Lu et al., 2020b).

In this study we focus on three proxies – benthic foraminiferal surface porosity, benthic foraminiferal I/Ca, and authigenic Uranium (aU) – on the same suite of globally distributed core-top sediments and a 30-kyr down-core record from within the Arabian Sea Oxygen Minimum Zone (OMZ). The OMZs in Arabian Sea contain one of the major water column denitrification zones in the world ocean, where nitrate is being reduced and ultimately produces  $N_2$  gas (Naqvi, 1987; Morrison et al., 1999). We first expand the global core-top calibration of benthic surface porosity and I/Ca proxies (Rathburn et al., 2018; Lu et al., 2020b) to further assess their relationships with BWO and discuss potential impacts of other non-oxygen factors. We also present a regional calibration of the aU proxy in the Arabian Sea region to assess its potential and limitations. We then evaluate consistency among glacial-Holocene BWO reconstructions using each of these proxies, as well as the  $\Delta\delta^{13}$ C proxy, in a sediment core taken from within the Arabian Sea OMZ.

## 1.1. Benthic foraminiferal surface porosity proxy

In low-oxygen environments, the surfaces of benthic foraminiferal tests show high porosity, which was suggested to be a biotic response to facilitate gas exchange (Bernhard, 1986; Kaiho, 1994). While several previous studies have linked pore patterns with ambient bottom water conditions (e.g., dissolved oxygen and nitrate concentrations) (Glock et al., 2011; Kuhnt et al.,

2013, 2014), the species studied were generally limited to shallow to deep infaunal species (e.g., *Bolivina spissa*, *Bolivina pacifica*, *Fursenkoina Mexicana*, *Chilostomella oolina*, *Globobulimina turgida*), which are more likely to be influenced by pore-water conditions. A methodology recently developed by Petersen et al. (2016) provides standardized procedures to quantify pore patterns. Rathburn et al. (2018) presented the first global calibration of surface porosity on live-collected epifaunal foraminifera (*Cibicidoides* spp. and *Planulina* sp.) and an equation to quantify BWO. However, as gas exchange may be only one of the functions of surface pores (Glock et al., 2012), it is uncertain whether and how other non-oxygen factors may impact the benthic surface porosity. In Section 5.1, we utilize published Arabian Sea seawater chemistry data from U.S. Joint Global Ocean Flux Study (JGOFS) to assess the potential impact of two other important pore functions – taking up organic carbon as food resources and releasing respiratory CO<sub>2</sub> – on benthic surface porosity.

## 1.2. Benthic I/Ca proxy

The I/Ca proxy is derived from the redox-sensitive behaviors of iodine species in the seawater. Two thermodynamically stable iodine species are the oxidized form iodate ([IO<sub>3</sub>-]) and the reduced form iodide ([I-]) (Wong and Brewer, 1977). Two major factors are thought to control the iodine species in seawater: 1) in situ redox processes: iodate reduction to iodide in anoxic conditions and iodide re-oxidation to iodate in oxic waters (Rue et al., 1997); and 2) regional water mass mixing: the diffusion/advection of water masses forming nearby with variable iodate concentrations (Hardisty et al., 2021). Iodate, substituting for carbonate ion (Podder et al., 2017; Feng and Redfern, 2018), is the only iodine species incorporated into the

calcite structure (Lu et al., 2010), and thus lower foraminiferal I/Ca values generally indicate lower seawater iodate concentrations. Broadly, low iodate concentrations are found predominantly within lower oxygen water masses that reflect iodate reduction close to the foraminiferal habitat (Lu et al., 2020a; Hardisty et al., 2021). However, the global relationship between I/Ca on live-collected and core-top benthic foraminifera and BWO is not linear. Instead, benthic I/Ca values below 3 µmol/mol generally are observed when BWO < 50 μmol/kg (Lu et al., 2020b). As benthic surface porosity measurements are non-destructive, I/Ca can be measured on the same suite of specimens after benthic surface porosity measurements are completed. Comparisons of benthic surface porosity and I/Ca in globally-distributed coretops and Southeast Atlantic down-core records suggest proxy consistency despite fundamentally different mechanisms by which low BWO (< 100 µmol/kg) influences each proxy (Lu et al., 2021). We extend this paired proxy approach to core-top and down-core samples from the Arabian Sea to test proxy consistency in a different setting. In addition, in Section 5.2, we also assess how non-oxygen factors (i.e., temperature, salinity, carbonate ion concentrations) may affect I/Ca on global and regional scales.

131

132

133

134

135

136

137

116

117

118

119

120

121

122

123

124

125

126

127

128

129

130

## 1.3. Authigenic uranium (aU) proxy

The aU proxy has been used as a qualitative indicator for sedimentary oxygen conditions (Bradtmiller et al., 2010; Jaccard et al., 2016; Jacobel et al., 2017, 2020; Costa et al., 2018). In oxygenated seawater, U occurs as soluble U(VI); as pore-water oxygen becomes depleted, soluble U(VI) reduces to insoluble U(IV) and precipitates as solid UO<sub>2</sub> (Anderson, 1982; Anderson et al., 1989; Morford and Emerson, 1999). The redox state of sedimentary aU is

mainly controlled by two factors: (1) the oxygen concentrations of overlaying bottom waters, and (2) the organic carbon flux to the sediments, which results in respiration and consumption of oxygen in porewaters (Bradtmiller et al., 2010). However, sedimentary aU accumulation can be impacted by post-depositional burndown and remobilization, i.e., it may be removed by subsequent reoxygenation at the sampling site (Jacobel et al., 2017; Costa et al., 2018). In Section 5.3, we evaluate the relationship of core-top aU data to BWO in the Arabian Sea region to assess its utility as a semi-quantitative proxy.

## 1.4. Carbon isotope gradient ( $\Delta \delta^{13}$ C) proxy

The  $\Delta\delta^{13}$ C has been calibrated from 20 µmol/kg to as high as 235 µmol/kg, and is the only quantitative BWO proxy that can reconstruct oxygen concentrations above 50 µmol/kg. The proxy is based on the assumption that more organic carbon remineralization within surface sediments releases isotopically lighter carbon into the pore-water and thus enhances the  $\delta^{13}$ C gradient between bottom water (recorded by  $\delta^{13}$ C $_{Cwuellerstorfi}$ ) and anoxic pore water (recorded by  $\delta^{13}$ C $_{Globobulimina}$ ) (McCorkle and Emerson, 1988; Hoogakker et al., 2015, 2018). However, the  $\delta^{13}$ C in the deep infaunal *Globobulimina* spp. may also be impacted by isotopically lighter  $\delta^{13}$ C released from anaerobic processes (i.e., sulfate reduction and denitrification), which would result in higher  $\Delta\delta^{13}$ C, and thus over-estimate BWO (Jacobel et al., 2020). To evaluate this hypothesis, we compare a glacial-Holocene  $\Delta\delta^{13}$ C-based BWO reconstruction from Arabian Sea OMZ to the BWO reconstructed from the three other proxies at the same site.

## 2. Samples and Methods

#### 2.1. Samples

160

161

162

163

164

165

166

167

168

169

170

171

172

173

174

175

176

A total of 70 core-top samples and 24 down-core samples were used in this study (Supplementary tables). All sediment samples were taken from Woods Hole Oceanographic Institution (WHOI) Seafloor Samples Repository. For the core-top calibrations, samples were taken from the top 5 cm of most cores. Cores TN041-8PG and 8JPC (17°48.76' N, 57°30.34'E, water depth 761 m) are from the center of modern Arabian Sea OMZ. Core 8PG was sampled every 16 cm from top to bottom (a total of 224 cm, extending to  $\sim$  15.6 kyr BP). We extended the record of 8PG to ~30 kyr BP using 8JPC, which was also sampled at 16 cm intervals. All samples were freeze-dried and then aliquoted for bulk sediment geochemistry analyses. The rest of sediments were wet-sieved to > 63 µm fraction with de-ionized water, and oven-dried at 45°C. Planktic foraminifera Globigerinoides ruber were picked from 250-355 µm fraction, and benthic foraminifera Cibicidoides spp., Planulina sp., and Globobulimina affinis were picked from the > 212 µm fraction. Note that in some samples Cibicidoides spp. and Planulina sp. were not found or not available in sufficient numbers for isotope or I/Ca analyses. Most of our core-top samples are from four regions: Eastern Equatorial Pacific (EEP, n = 10), Arabian Sea (n = 28), Little Bahamas Bank (LBB, n = 14), and Demerara Rise (DR, n = 11), as outlined in dashed boxes in Fig. 1.

177

178

179

180

181

## 2.2. Age constraints and stable isotopes

All core-top samples have near-modern or late Holocene ages, based on published ages from nearby cores or online cruise reports (Supplementary Table). No identification of living vs. dead benthic foraminifera specimens was made in the core-top samples. Ages of TN041-

8PG/8JPC were first estimated using the  $\delta^{18}$ O stratigraphy of *G. ruber*, then 7 samples were selected for radiocarbon dating. Each radiocarbon date represents an average of 300-350 individuals of *G. ruber*, picked from the > 250 or > 335  $\mu$ m size fractions. All accelerator mass spectrometry (AMS) <sup>14</sup>C dates were acquired at the National Ocean Sciences Accelerator Mass Spectrometry facility at WHOI. Planktic <sup>14</sup>C dates were calibrated against Marine20 using Calib8.20 (Stuiver et al., 2022) using an Arabian Sea regional marine radiocarbon reservoir age correction  $\Delta R = 93$  and uncertainty of 61 (Heaton et al., 2020) (Table 2). The age model was then constructed using the BACON v2.3.91 package in R (Blaauw and Christen, 2011) (Fig. S1).

Carbon and oxygen isotopic analyses were made using a Finnigan MAT253 mass spectrometer at WHOI with a long-term laboratory precision (1 $\sigma$ ) of the NBS-19 carbonate standard of  $\pm$  0.07 ‰ for  $\delta^{18}$ O and  $\pm$  0.02 ‰ for  $\delta^{13}$ C (Umling et al., 2019). The isotopes on *Cibicidoides* spp. were performed after benthic surface porosity analyses were completed. Each isotope analysis used 4 – 5 specimens of *G. ruber*, 2 specimens of *Cibicidoides* spp., and 2 specimens of *G. affinis*.

# 2.3. Foraminiferal surface porosity

We measured the surface porosity of benthic foraminifera following Petersen et al. (2016). We focused on *Cibicidoides* spp. and *Planulina* sp. because they are thought to be epifaunal or shallow infaunal species, thus more likely to record bottom water or shallow pore-water conditions (Rathburn et al., 2018), while deep infaunal species are likely to record more reducing pore-water conditions. Additionally, *Cibicidoides* spp. and *Planulina* sp. are widely

distributed and found alive in a wide range of BWO between ~2 and ~277 µmol/L, therefore can be broadly applied in paleoceanographic records (Rathburn et al., 2018). Around 1-8 specimens of each benthic species were analyzed, for a total of 137 individuals in 33 core-top samples, 73 individuals in 15 down-core samples in TN041-8PG, and 32 individuals in 6 downcore samples in TN041-8JPC. Photos were taken using a Scanning Electron Microscope (SEM) (Hitachi model TM3000) at WHOI. The dorsal side of each specimen (side that is exposed to bottom water) was imaged. ImageJ, a semi-automatic image-processing software (available at https://imagej.nih.gov/ij/), was then used to calculate the surface porosity, based on a grayscale threshold applied to a specific frame. Because the last chamber is often broken or absent, porosity was calculated for the penultimate chamber of all specimens, which represents the same ontogenetic stage. The frame was placed in an area representative of the whole chamber, usually the inner, flat portion of the chamber, to avoid including distorted pores. Frames were manually positioned using a macro developed by Petersen et al. (2016), which allowed us to place a frame of the same size on all SEM images. Selected representative SEM photos of benthic foraminifera of *Cibicidoides* spp. and *Planulina* sp. are shown in Fig. S2.

204

205

206

207

208

209

210

211

212

213

214

215

216

217

218

219

220

221

222

223

224

225

Three different frame sizes were first tested to choose the best frame representing the porosity of the chambers. They were tested initially on four randomly chosen foraminiferal specimens (two small foraminifera (300-350 µm in diameter) and two large foraminifera (1000-1200 µm in diameter)), then applied to the rest of the samples. A non-parametric analysis (Kolmogorov-Smirnov) following the method of Petersen et al. (2016), was carried out on the porosity data of three different frames to test the distribution of the data, helping to determine which frame would be the most suitable for the species used. Subsequently, the same fixed

frame size was applied to all photos analyzed. The porosity was reported as the average of 1-8 specimens per sample. The standard deviations ( $1\sigma$ ) of porosity are usually higher in samples with high porosity (i.e., 3-16%) than those with low porosity (i.e., 0-4%).

229

230

231

232

233

234

235

236

237

238

239

240

241

242

243

244

245

246

247

226

227

228

#### 2.4.Foraminiferal I/Ca

After the porosity and isotope measurements were completed, I/Ca analyses were performed on 4-16 remaining specimens, following Lu et al. (2020b). The foraminiferal cleaning method was modified from the Mg/Ca protocol (Barker et al., 2003). The samples were gently crushed using cleaned glass slides to open all chambers. Samples were then cleaned by ultrasonication in de-ionized water to remove clays, a 10 - 20 min boiling-water bath in NaOH-buffered 1% H<sub>2</sub>O<sub>2</sub> solution to remove organic matter, and three additional rinses with de-ionized water. A reductive cleaning step was not applied because Mn oxides contain negligible amount of iodine (Zhou et al., 2014). The cleaned samples were dissolved in 3% HNO<sub>3</sub>, then diluted to solutions containing ~50 ppm Ca, 5 ppb internal standards (Sc, In, Cs), 0.5% tetramethylammonium hydroxide (to stabilize iodine), and 0.5% HNO<sub>3</sub> (to avoid clogging the nebulizer). The measurements were performed immediately on a Thermo Scientific iCAP Qc ICP-MS at WHOI. Calibration standards were freshly made for each batch of samples. Consistency was monitored through repeated analyses of the reference coral standard JCp-1 between every 3 unknown samples. The I/Ca value of JCp-1 for all batches measured at WHOI is  $4.20 \pm 0.30 \,\mu\text{mol/mol}$  ( $1\sigma$ , n = 72), consistent with  $4.27 \pm 0.06 \,\mu\text{mol/mol}$  $(1\sigma, n = 8)$  reported in Lu et al. (2010) and suggesting an external reproducibility of ~7% (1 $\sigma$ ). Replicates of selected samples yielded a reproducibility ranging from  $\pm 0.1 \, \mu mol/mol \, (1\sigma)$  to

249

250

251

252

253

254

255

256

257

258

259

260

261

262

263

264

265

266

267

268

269

#### 2.5. Bulk sediment trace elements

For bulk trace element analyses, ~10 mg of bulk freeze-dried samples was digested using a mixture of nitric acid (HNO<sub>3</sub>, 1 mL), hydrofluoric acid (HF, 1 mL), and hydrochloric acid (HCl, 0.1 mL) at 135 °C. Aqua regia was then used to break down fluorides formed during the HF digestion. The dried sample was redissolved in 2% HNO<sub>3</sub> and diluted prior to analyses on the Thermo iCAP Q ICP-MS at WHOI. Two standard calibration curves were run at the beginning and the end of the analyses, including rock (BHVO-2 [basalt] and AGV-2 [andesite], United States Geological Survey) and the high-purity ICP-MS standards. Indium was used as an internal standard to monitor the instrument drift. MESS-3 (continental margin sediments) from the National Research Council of Canada was used as the standard reference material to monitor accuracy, which yielded an external recovery of 96-113% for all certified trace elements. Relative standard deviation (RSD) for the five measurements of each sample was <10%. The sedimentary U concentrations can be influenced by several processes, including but

not limited to redox, lithogenic input, and hydrothermal activities. No active hydrothermal vents are found or known to exist close to the Arabian Sea transect (Beaulieu et al., 2013; German and Seyfried, 2013). Thus, a hydrothermal metal component in the Arabian Sea transect is unlikely.

The lithogenic U was calculated using a detrital <sup>238</sup>U/<sup>232</sup>Th activity ratio of 0.7 in Arabian Sea, a basin-average value as recommended by Henderson and Anderson (2003) and

commonly used in the studied regions (Costa et al., 2020). As shown in Section 5.3, apatite may have contributed to a significant amount of U in bulk sediments, thus we corrected apatite-bound U. Because apatite fraction in solid P phases was ~80% in Arabian Sea based on sequential chemical extraction results (Schenau et al., 2000; 2005), we first calculated P content from apatite:

- Apatite-bound-P = apatite fraction in solid P phases \* total P (wt.%) (1)
- Next, we converted the P content to grams of apatite, using 18.25 wt.% P content of apatite:
- 277  $M_{apatite} = Apatite-bound-P / 18.25 (wt.\%)$  (2)
- Next, we converted the grams of apatite to apatite-bound U, using an estimated U in apatite of
- 279 75 ppm (average U concentrations in Pliocene-Holocene phosphorites) (Baturin and Kochenov,
- 280 2001).

284

285

286

287

288

289

290

291

270

271

272

273

274

- Apatite-bound-U (ppm) =  $M_{apatite} * U$ -in-apatite (ppm) (3)
- Lastly aU was calculated by total U subtracting lithogenic U and apatite-bound U.
- aU (ppm) =  $U_{total}$  Th \* (U/Th)<sub>detrital</sub> Apatite-bound-U (4)

## 2.6. Total organic carbon (TOC)

For total organic carbon (TOC) in the bulk sediments, 2-10 mg freeze-dried samples were weighed into pre-cleaned silver boats and acidified using 2N HCl. Acidified samples were then dried and analyzed on a Carlo Erba Elemental Analyzer 1108 in the Organic Mass Spectrum Facility at WHOI. USGS-40 (L-glutamic acid, C = 40.8 wt. %) and glycine (C = 32.0 wt. %) were used as standards. All measurements were conducted in triplicate.

We used dissolved TOC concentrations in seawater (TOCsw, which includes both

particulate and dissolved organic matter), reported from six Arabian Sea Joint Global Ocean Flux Study (JGOFS) cruises archived in the US-JGOFS database (<a href="http://usigofs.whoi.edu/datasys/mrg/mrgdir.html">http://usigofs.whoi.edu/datasys/mrg/mrgdir.html</a>). Details on analyzing TOC<sub>SW</sub> were reported in Hansell and Peltzer (1998). We extracted the TOC<sub>SW</sub> data from the nearest cruise station to our Arabian Sea core tops (Supplementary Table).

# 2.7. Hydrographic data

The oxygen data were extracted from the nearest site in the JGOFS database (Arabian Sea transect) or World Ocean Atlas (WOA) 2018 (Garcia et al., 2019). Temperature and salinity for core-top sites were obtained from JGOFS database (Arabian Sea transect), cruise report (DR transect), or from Rosenthal et al. (2006) (LBB transect), or the nearest site in WOA2018. Dissolved inorganic carbon (DIC), total alkalinity, and anthropogenic CO<sub>2</sub> were obtained from the sites closest to the core sites using the GLODAP dataset (version 1.1) (Key et al., 2004). The anthropogenic CO<sub>2</sub> contribution was removed from DIC. We calculated preindustrial [CO<sub>3</sub><sup>2-</sup>] for calcite using the CO2sys.xls program (Pelletier et al., 2005).

## 3. Results

## 3.1. Core-top for a miniferal surface porosity

Globally, high benthic surface porosity (> ~10%) is associated with low-BWO samples (i.e., < ~50  $\mu$ mol/kg), while low porosity or no pores are found on the foraminiferal surfaces from high-BWO samples (50 – 300  $\mu$ mol/kg) (Fig. 2), consistent with a previous study on live-collected foraminifera (Rathburn et al., 2018). No systematic porosity differences are found

among different Cibicidoides spp. from the same location.

In the depth profile of EEP, benthic surface porosity is the highest (33 - 35%) at OMZ depths (~400 m), then decreases with increasing water depths, and reaches < 5% in higher BWO at 1500-3000 m (Fig. 3). The porosity depth profile in the Arabian Sea is similar to the EEP, with the highest value of ~36% at OMZ depths of ~600 m, decreasing with increasing water depths, reaching low values (0 - 5%) at ~2000 m, and remaining consistently low below 2000 m.

Globally, higher porosity is generally associated with higher TOC in sediments ( $R^2 = 0.71$ , p < 0.01, Fig. 4A). However, this correlation may be spurious because TOC<sub>sed</sub> is negatively correlated with BWO ( $R^2 = 0.61$ , p < 0.01, Fig. 4B). In the Arabian Sea, benthic surface porosity does not exhibit a strong correlation with TOC<sub>sw</sub> ( $R^2 = 0.21$ , p = 0.04) (Fig. 4C). Benthic surface porosity shows a general inverse relationship with TCO2<sub>sw</sub> ( $R^2 = 0.57$ , p < 0.01, Fig. 4D), which may be due to the correlation between TCO2<sub>sw</sub> and BWO when BWO is low ( $< 100 \, \mu \text{mol/kg}$ ) ( $R^2 = 0.93$ , p < 0.01, Fig. 4E).

## 3.2.Core-top benthic I/Ca

Globally, low benthic I/Ca values (0 – 3 μmol/mol) are only found in low-BWO waters (< 50 μmol/kg), while I/Ca values show large variations (3 – 22 μmol/mol) in high-BWO sites (> 50 μmol/kg) (Fig. 5A). Little or no relationship between I/Ca vs. temperature, salinity, and [CO<sub>3</sub><sup>2-</sup>] is found in the global core-top dataset. Benthic I/Ca and BWO are not linearly correlated in the transects from any of the four investigated regions (Fig. S3). Note that although the error bars are sometimes higher at low I/Ca ranges (i.e., 8-18%), the overall range

of I/Ca variations is much larger than the error bars (Fig. 5).

The I/Ca values from waters spanning a small BWO range are compared with non-oxygen parameters (Fig. 5B). In the LBB transect, where BWO ranges between 150 and 200  $\mu$ mol/kg, I/Ca has an inverse relationship with bottom water temperature, salinity, and [CO<sub>3</sub><sup>2-</sup>]. In the EEP transect, where BWO ranges between 0 and 50  $\mu$ mol/kg, I/Ca does not appear to correlate with temperature, salinity, or [CO<sub>3</sub><sup>2-</sup>], although the sample size of the dataset is small (n = 5). In the depth profiles of EEP and Arabian Sea, I/Ca is < 3  $\mu$ mol/mol in the OMZ depths (~200 m to 600 m in EEP and ~200 to 800 m in Arabian Sea), and becomes variable, ranging between 4 and 12  $\mu$ mol/mol with increasing water depth (Fig. 6).

#### 3.3.Core-top aU

In the Arabian Sea, the total U concentrations spread a wide range, from 0.7 ppm to 63.4 ppm (Supplementary table). Two multicores (TOM47-1-MC26D and MC26F) show remarkably high U concentrations (34.2 and 63.4 ppm, respectively) and also high P contents (4.4 and 10.8 wt.%, respectively). The cross-plot suggests that  $U_{total}$ /Th<sub>total</sub> is highly correlated with P<sub>total</sub>/Al<sub>total</sub> ( $R^2 = 0.97$ ) (Fig. 7A). As will be discussed below in Section 5.3, apatite may have contributed a large amount of U to the OMZ sediments in Arabian Sea, thus the correction of apatite-bound U was applied to calculate the actual aU that is potentially related to BWO. After correcting the apatite-bound U, elevated aU (> 3 ppm) is found in waters with oxygen < 10 µmol/kg, while relatively lower aU is found in better-oxygenated samples (Fig. 8). A statistical method called "receiver operating characteristic" (Zou et al., 2007) was applied to determine the aU threshold for BWO < 30 µmol/kg in Arabian Sea. The statistical results show

that to best classify the presence/absence of low-BWO (< 30 µmol/kg), the optimal aU threshold should be  $\sim$ 3, with true-positive rate (i.e., the proportion of low-BWO correctly identified as low-BWO) of 100% and low false-positive rate (i.e., the proportion of high-BWO incorrectly identified as low-BWO) of 0%. We note that this aU threshold value is only for Arabian Sea and does not apply to other regional or global scales.

# 3.4. Multi-proxy records from core TN041-8PG/8JPC

Benthic surface porosity in *Cibicidoides* spp.and *Planulina* sp. is consistently high (20 – 40%) throughout the 30-kyr-long record (Fig. S4). Benthic surface porosity was relatively lower (~20 %) in the glacial period between 30 and 18 ka, increased during the deglaciation between 18 and 12 ka, and remained 30 - 40 % during the Holocene. The I/Ca values are relatively constant throughout the record, ranging between 2 and 2.5  $\mu$ mol/mol (Fig. 9). Because  $U_{total}/Th_{total}$  is also highly correlated with  $P_{total}/Al_{total}$  ( $R^2 = 0.83$ ) in down-core samples (Fig. 7B), we also corrected for the apatite-bound U. The aU concentrations are > 3 ppm throughout the record (Fig. 9). Relatively higher (6 – 11 ppm) aU is found between 31 and 27 ka, decreasing to 3 - 6 ppm between 27 and 11 ka, increasing to 12 ppm during early Holocene, and then finally decreasing to 6 ppm during late Holocene. The aU flux estimates show similar high background values and temporal trends as aU concentrations (Fig. S5).

The  $\delta^{13}$ C values of *Cibicidoides* spp. are ~0.5 ‰ in the glacial period. They are highly variable during the deglaciation, and exhibit a slight increase from 0.23‰ in early Holocene to 0.41‰ in late Holocene (Fig. S4). The  $\delta^{13}$ C in *G. affinis* remains around -0.8‰ throughout the glaciation and deglaciation and increases to -0.2‰ at ~3.4 ka. The  $\Delta\delta^{13}$ C values scatter between

0.6 and 1.4 ‰ throughout the record, except one sample having a low value (0.4‰) at 6.6 ka (Fig. 9).

#### 4. Discussion

The new globally distributed core-top benthic foraminiferal surface porosity and I/Ca data reported in this study are consistent with previous studies (Glock et al., 2014; Rathburn et al., 2018; Lu et al., 2020b), with most high porosity and low I/Ca found in the low-oxygen waters (< 50 µmol/kg) in the EEP and Arabian Sea. A strong relationship between aU and BWO is apparent in the Arabian Sea. Our results suggest that each proxy has both potential and limitations.

## 4.1. Controls on benthic foraminiferal surface porosity

Surface pores on foraminiferal tests are thought to be used for both gas exchange and for taking up organic carbon as food resources (Glock et al., 2012). The surface porosity in live-collected benthic foraminifera (living attached on hard surfaces such as rocks and manually removed on the ship, or stained with Rose Bengal with conservative assessments) is correlated with TOC content in the sediments due to the anti-correlation between TOC<sub>sed</sub> and BWO (Rathburn et al., 2018). These correlations are also observed in our core-top dataset (Fig. 4A-B). The TOC content in sediments is influenced not only by BWO, but also by export productivity, organic carbon respiration, dilution, and preservation in the sediments (Canfield, 1994; Tyson, 2001; Schoepfer et al., 2015). In the Arabian Sea, TOC<sub>sed</sub> exhibits a different depth profile from TOC<sub>sw</sub> (Fig. 3B), suggesting that factors other than export production affect

the concentrations of TOC<sub>sed</sub>.

The TOCsw is a more direct indicator of food availability in the water column. The correlation between TOCsw and benthic surface porosity in the Arabian Sea transect is weak  $(R^2 = 0.21, Fig. 4C)$ , suggesting that dissolved organic carbon availability in the seawater does not significantly impact the benthic surface porosity.

While gas exchange is thought to be an important function of surface pores, pores may also be used to release respiratory CO<sub>2</sub> (Glock et al., 2012). However, there is a general inverse relationship between TCO2sw and benthic surface porosity (Fig. 4D), opposite to what is expected if higher porosity is linked to more CO<sub>2</sub> released to the seawater. Instead, the inverse relationship between TCO2sw and porosity may be a byproduct of correlation between TCO2sw and BWO when BWO < 100  $\mu$ mol/kg (Fig. 4E) as higher CO<sub>2</sub> in the seawater linked to more oxic respiration.

In summary, benthic surface porosity does not seem to have direct connections with organic carbon availability or TCO2 concentrations in the seawater, and thus BWO variability is likely the predominant control on benthic surface porosity. The relationships between benthic surface porosity and BWO when BWO <  $100 \mu mol/kg$  can be updated as follows (Fig. 2):

- Global:  $\ln(porosity) = 4.16 \pm 0.25 0.04 \pm 0.004 *BWO (R^2 = 0.67, p < 0.01, n = 40)$
- 420 Arabian Sea:  $ln(porosity) = 3.62 \pm 0.16 0.03 \pm 0.003*BWO (R^2 = 0.89, p < 0.01, n = 11)$

where the unit of porosity is in %. The uncertainties associated with reconstructing BWO from the global core-top dataset are about  $\pm 10~\mu mol/kg$  at 20  $\mu mol/kg$  (with average porosity S.D.

of 8%) and increase to  $\pm 33 \, \mu mol/kg$  at 80  $\mu mol/kg$  (with average porosity S.D. of 2%).

#### 4.2. Controls on benthic I/Ca

In the global core-top dataset, the relationship between I/Ca and BWO appears to be more robust than the relationship with other environmental variables (Fig. 5A). Benthic I/Ca does not show linear or logarithmic relationships with BWO globally or in any of the four studied regions (Fig. S3). The most robust feature in the global dataset is that low benthic I/Ca < 3 µmol/mol are exclusively found in low-BWO sites (< 50 µmol/kg). The low I/Ca values are assumed to track low iodate concentrations in seawater (Lu et al., 2010), which could originate from in situ iodate reduction in low-BWO waters and/or regional diffusion/convection of low iodate seawater from nearby low-BWO water masses (Hardisty et al., 2021). Thus the low I/Ca values could be used to indicate the presence of low-BWO < 50 µmol/kg waters from a small spatial scale, consistent with previous work (Lu et al., 2020b).

To further consider non-BWO effects, we evaluate I/Ca data from regional samples within a small BWO range (150 – 200 μmol/kg in the LBB transect; 0 – 50 μmol/kg in the EEP transect). In the low-BWO EEP region, I/Ca does not show a significant relationship with temperature, salinity, or [CO<sub>3</sub><sup>2</sup>-]. In the high-BWO LBB transect, inverse relationships are found between I/Ca and temperature, salinity, and [CO<sub>3</sub><sup>2</sup>-] (Fig. 5B). An inverse relationship between I/Ca and temperature has been previously reported in inorganic calcite synthesis experiments in the laboratory (blue dash line shown in Fig. 5) (Zhou et al., 2014). The core-top data appear to fall along the temperature-I/Ca laboratory curve at higher temperatures between 12 and 17°C, but they are above the curve at lower temperatures, between 5 and 12°C. The

deviation becomes larger at lower temperatures. We speculate that biological factors may play a larger role in controlling the iodine incorporation into foraminiferal test at lower temperatures, e.g., perhaps iodate is preferentially incorporated into the foraminiferal shell at lower temperatures. The I/Ca are also inversely related to salinity and  $[CO_3^{2-}]$ , which may be an artifact of the positive relationship between temperature and salinity  $(R^2 = 0.97)$  and  $[CO_3^{2-}]$   $(R^2 = 0.93)$  in the LBB region. Alternatively, higher I/Ca are associated with lower  $[CO_3^{2-}]$ , suggesting that when ambient seawater has less  $[CO_3^{2-}]$  availability, foraminifera may more readily substitute  $[IO_3^{-}]$  into the calcite structure thus resulting higher I/Ca.

Most low I/Ca < 3  $\mu$ mol/mol are found in OMZ samples with BWO < ~10  $\mu$ mol/kg in the EEP and Arabian Sea (Fig. S3). Compiled seawater iodate data from nearby EEP stations off Peru (Cutter et al., 2018) and Arabian Sea stations (Farrenkopf et al., 1997; Farrenkopf and Luther, 2002) suggest that iodate reduction mainly (although not always) occurs in the depths between ~50 and ~500 m in EEP (Fig. 6A) and between ~200 and ~800 m in Arabian Sea (Fig. 6B), coinciding with the depths of denitrification layer (oxygen < ~10  $\mu$ mol/kg) (Naqvi, 1987; Morrison et al., 1999). As water column denitrification preferentially removes  $^{14}$ N, leaving the residual nitrate enriched in  $^{15}$ N, the denitrification layer is identified by elevated nitrite concentrations and higher  $\delta^{15}$ N of nitrate (Cline and Kaplan, 1975; Brandes et al., 1998; Altabet et al., 1999). The close link between iodate reduction and denitrification zones may be because the same bacteria and enzymes responsible for denitrification are also capable of iodate reduction (Tsunogai and Sase, 1969; Wong and Hung, 2001). Although iodate reduction may be linked to denitrification, we note that the iodate reduction does not always occur in the denitrification layer as observed in Arabian Sea, Eastern Tropical South Pacific (Fig. 6), and

Eastern Tropical North Pacific OMZs (Moriyasu et al., 2020; Hardisty et al., 2021), due to variable iodate reduction rates and influences of water mass mixing. Thus the presence of low  $I/Ca < 3 \mu mol/mol$  could be a useful indicator for denitrification processes, however, high  $I/Ca > 3 \mu mol/mol$  does not necessarily suggest the absence of denitrification processes.

Outside the denitrification layer in EEP and Arabian Sea, iodate concentrations are equivalent to global mean concentrations in oxic waters (Fig. 6), suggesting limited or no iodate reduction in deeper waters (Farrenkopf et al., 1997; Farrenkopf and Luther, 2002; Cutter et al., 2018). In Arabian Sea, foraminiferal I/Ca shows a wide range, between 4 and 11 µmol/mol, at 1000 - 1500 m, despite low BWO < 50 µmol/kg in these depths. We speculate that higher I/Ca values reflect higher iodate concentrations in ambient seawater. Globally, iodate concentrations in oxic seawater are mostly uniform (~500 nM) (Chance et al., 2014). While several stations in the Arabian Sea have iodate concentrations consistent with global oxic seawater (e.g., TY92-411, 481, 493 in Fig. 6B), some sites have total iodine concentrations > 500 nM (e.g., TN050-S7 in Fig. 6B), possibly sourced from high iodine released from marginal sediments and associated pore waters (Farrenkopf and Luther, 2002). Such spatial variability of seawater iodate may explain higher I/Ca in some samples, thus limiting the usage of higher I/Ca > 3 µmol/mol to infer specific BWO values, although future work on parallel analyses on seawater oxygen, iodine species, and I/Ca at the same location are required to confirm this hypothesis.

## 4.3. Controls on sedimentary U in Arabian Sea

In the Arabian Sea, remarkably high total U concentrations (maximum of 63.4 ppm) are found in the OMZ sediments. Previously high U (> 10 ppm, maximum of 32 ppm) had been

reported in surface sediments on the Oman Margin and coastal areas (Shankar et al., 1987; Sirocko et al., 2000), where samples with U > 10 ppm in this study are also located (Fig. S6). Note that not all samples located on the Oman Margin have high U > 10 ppm. The exceptionally high U on the Oman Margin was interpreted to be caused by both anoxic conditions and the presence of abundant fish remains (biogenic apatite), which generally contain high U concentrations (Shankar et al., 1987). Indeed, abundant fish debris were found in the sediments in Arabian Sea OMZ (Schenau et al., 2000). High P contents (up to 2 wt.%) were reported in the surface sediments from a site on Oman Margin (BC484, 19.5°N, 58.43°E, water depth 527 m), of which ~80% were consisted of authigenic carbonate fluoroapatite and biogenic apatite (fish debris) based on sequential chemical extraction results (Schenau et al., 2000). The P content is also high in our OMZ samples on Oman Margin with a maximum of 10.8 wt.% (red and yellow symbols in Fig. 7A). Thus apatite was likely present in these samples and adding U into the sediments independently of BWO.

We then correct the apatite-bound U to calculate the actual authigenic U that is potentially related to BWO (see calculations in Section 3.5). Assuming an average of 75 ppm U in apatite minerals (Baturin and Kochenov, 2010), the calculations suggest apatite could contribute 6 – 56% of total U in the sediments. As the equation (3) in Section 3.5 indicates, a large uncertainty of the apatite correction method comes from U concentrations in apatite minerals, which shows a large variation in natural samples. We subsequently perform a simple sensitivity test, using a minimum of 3 ppm and a maximum of 120 ppm U derived from modern nonlithified phosphatic concretions from the surficial sediment layers (Baturin and Kochenov, 2010). Results suggest that using different U concentration in apatite minerals for correction would change the

absolute values of aU, however, relatively higher aU are still exclusively found in OMZ depths in the Arabian Sea (Fig. S7A-C). Another uncertainty of the apatite correction method comes from the assumption that apatite fraction in solid P phases is  $\sim$ 80% in all samples (equation (1)) (Schenau et al., 2000). We additionally use an independent method to calculate apatite-bound P by using total P subtracting detrital P (utilizing Al content and P/Al ratio from upper crust) (Rudnick and Gao, 2003), organic-bound P (utilizing TOC<sub>sed</sub> and Redfield ratio of P:Corg) (Anderson and Sarmiento, 1994), and Fe-bound P (utilizing 12% fraction found in deep Arabian Sea sediments) (Schenau et al., 2000, 2005) in a subset of core-top samples (Fig. S7D). The calculations suggest apatite contributes to  $65\pm22$ % of the total P, consistent with the estimates from sequential chemical extraction results (Schenau et al., 2000). In four correction methods, the aU threshold for low BWO < 30  $\mu$ mol/kg are around 3 ppm. Because redox and productivity processes are closely coupled in the Arabian Sea (Schenau et al. 2005; Altabet et al., 2002), we conclude that high aU in Arabian Sea is primarily controlled by redox conditions which are in turn driven by high export production.

## 4.4. Down-core comparison in Arabian Sea

We compare BWO reconstructions based on benthic surface porosity, I/Ca, aU, and Δδ<sup>13</sup>C at down-core TN041-8PG/8JPC from the modern Arabian Sea OMZ center (water depth 761 m) to evaluate proxy consistency during the last ~30 kyr (Fig. 9). The Arabian Sea core-top porosity calibration equation (Section 5.1) was applied to calculate the BWO concentrations at TN041-8PG/8JPC (note that using the global calibration equation produces similar calculated BWO concentrations). When samples have only one specimen (open symbols), we assumed a

standard error of  $\pm 8\%$  for porosity measurement (average SD in all samples). The porosity-based BWO estimates are ~20 µmol/kg in the glacial period, gradually decreasing to ~10 µmol/kg during deglaciation, and remaining <10 µmol/kg during the Holocene.

The I/Ca values are consistently < 3 µmol/mol, suggesting BWO < 50 µmol/kg (in a small regional scale) throughout the last ~30 kyr, consistent with the porosity proxy. We caution that the relatively constant I/Ca records cannot be interpreted to reflect stable oxygenation conditions, because low I/Ca could track low iodate in the seawater, but it is not directly correlated with in situ oxygen concentrations due to highly variable iodate reduction rates (Moriyasu et al., 2020; Hardisty et al., 2021). In addition, the threshold behavior of the I/Ca proxy may limit its ability to record subtle changes in low BWO conditions < 50 µmol/kg.

The down-core high background values of aU (> 3 ppm) fall into the low BWO ranges (<30  $\mu$ mol/kg) based on the Arabian Sea core-top calibration (Fig. 8). The relatively lower aU during the glaciation and deglaciation compared to Holocene suggests generally higher BWO, consistent with porosity-based BWO estimates.

Except for two samples at 6.6 and 3.4 ka, the down-core  $\Delta\delta^{13}$ C-based BWO values using calibration equation by Hoogakker et al. (2015) are consistently > 50 µmol/kg, much higher than those suggested by benthic surface porosity, I/Ca, and aU proxies. The  $\Delta\delta^{13}$ C are determined by  $\delta^{13}$ C in both *Cibicidoides* spp. and *G. affinis*. On the one hand, the *Cibicidoides* spp. used in this study is not *C. wuellerstorfi* (Fig. S2), thus its microhabitat could be epifaunal to shallow infaunal. If the *Cibicidoides* spp. were indeed shallow infaunal, the  $\delta^{13}$ C<sub>cibs</sub> could be 0.2 – 1 ‰ lower than the actual  $\delta^{13}$ C<sub>DIC</sub> in bottom waters (McCorkle et al., 1997; Fontanier et al., 2006), and this  $\delta^{13}$ C offset may have been larger during the glacial period (Gottschalk et

al., 2016). Thus, the actual glacial  $\Delta\delta^{13}C$  between bottom-water and anoxic pore-water might have been even larger than the  $\Delta\delta^{13}C$  we measured, suggesting even higher glacial BWO, and exacerbating the discrepancy with other proxy reconstructions.

On the other hand, it has been suggested that *G. affinis* can denitrify, i.e., it can respire with both oxygen and nitrate (Piña-Ochoa et al., 2010; Jacobel et al., 2020). The  $\delta^{13}$ C in *G. affinis* could thus be impacted by the lower  $\delta^{13}$ C released from both denitrification processes and the upward diffusion of light carbon from sulfate reduction within the sediments, and such offsets are likely larger in high productivity and low BWO sites (McCorkle and Emerson, 1988; Jacobel et al., 2020). Previous studies on pore-water geochemistry in the cores within the Arabian Sea OMZs have demonstrated that early diagenesis processes in top ~10 cm of sediments involve Fe-(hydr)oxides reduction and sulfate reduction (Passier et al., 1997), both of which could release low- $\delta^{13}$ C carbon into the pore waters. Denitrification processes within the Arabian Sea sediments were likely limited because most nitrate was used either in the water column and/or at the top of sediments (van der Weijden et al., 1999). But the downward diffusion of low- $\delta^{13}$ C released from bottom water denitrification can contribute to lower  $\delta^{13}$ C in pore waters. Thus the sediment diagenesis impact on  $\delta^{13}$ C *G.affinis* may explain the overestimation of  $\Delta\delta^{13}$ C-based BWO at this Arabian Sea OMZ site.

Finally, we compare the multi-proxy record in this study with the bulk sedimentary  $\delta^{15}N$  composite record from 5 cores located in Oman upwelling regions (Gaye et al., 2018) (Fig. 9). In the Arabian Sea, lower glacial bulk sedimentary  $\delta^{15}N$  values were interpreted to indicate less denitrification and a weaker or inactive glacial OMZ (Altabet et al., 2002; Gaye et al., 2018). The lower glacial benthic surface porosity and lower glacial aU are consistent with lower  $\delta^{15}N$ 

values, thus providing new, compelling evidence of a weaker OMZ in the glacial Arabian Sea compared to Holocene. In addition, since iodate reduction processes are closely coupled with denitrification in the modern OMZs (Section 5.2), the occurrence of low glacial I/Ca values < 3 μmol/mol suggests that denitrification still occurred during the glacial period, though possibly with lower rates. Finally, and perhaps most importantly, the benthic surface porosity record provides the first quantitative estimate of glacial BWO in the Arabian Sea, ~10 to ~15 μmol/kg higher than the Holocene.

#### 5. Conclusions

In this study we have evaluated three BWO proxies (benthic surface porosity, I/Ca, aU) in core-top samples on global and regional scales and compared glacial-Holocene BWO reconstructions using these proxies and  $\Delta\delta^{13}$ C proxy in a sediment core from within Arabian Sea OMZ. Four main findings are:

- 1) Globally, benthic surface porosity is primarily controlled by BWO when BWO < 100  $\mu$ mol/kg. In the Arabian Sea, benthic surface porosity appears independent from organic carbon availability and TCO2 concentrations in the water column.
- 2) Globally, the relationship between I/Ca and BWO is more robust than the relationship with other environmental variables. In the high-BWO LBB region, where BWO is not expected to control benthic I/Ca, benthic I/Ca appears negatively correlated with temperature, salinity, and [CO<sub>3</sub><sup>2-</sup>]. In the low-BWO EEP region, I/Ca does not show significant relationship with temperature, salinity, and [CO<sub>3</sub><sup>2-</sup>]. In both EEP and Arabian Sea, low I/Ca < 3 μmol/mol appears to track iodate reduction occurring within the denitrification layer; higher I/Ca > 3 μmol/mol may be related to spatial variability of

#### seawater iodate thus limiting its direct link to specific BWO values.

- 3) In the Arabian Sea, some OMZ samples have exceptionally high total U concentrations (> 10 ppm). High P content is also found in these samples, suggesting the presence of apatite. The addition of U from apatite could increase the total U in sediments independently of BWO. After correcting for apatite-bound U, high aU > 3 ppm are only found in low BWO waters < 30  $\mu$ mol/kg, which are ultimately driven by high export production in Arabian Sea.
- 4) The inter-comparison of BWO reconstructions based on benthic surface porosity, I/Ca, and aU in a 30-kyr core from the Arabian Sea OMZ reveals consistency, with all reconstructions suggesting BWO < 50  $\mu$ mol/kg throughout the record. The  $\Delta\delta^{13}$ C proxy, however, greatly over-estimates the BWO due to the potential impact of sediment diagenesis on  $\delta^{13}$ C<sub>G.affinis</sub>. The benthic surface porosity records further suggest glacial BWO may have been 10 15  $\mu$ mol/kg higher in Arabian Sea OMZ than the Holocene.

#### Acknowledgements

We thank the WHOI Seafloor Samples Repository for curating and providing the samples, and WHOI NOSAMS for radiocarbon analyses. We thank K. Pietro, G. Swarr, E. Roosen, and B. Monteleone for technical assistance, Z. Lu for discussions of I/Ca results. This work was funded by NSF grant OCE-1946185 (K.M.C., D.O.), OCE-1829406 (S.G.N.), WHOI Academic Programs Endowed Funds (D.O.). W.L. and Y. W. were supported by the WHOI Postdoctoral Scholar Program, with funding provided by the Weston Howland Jr. Postdoctoral Scholarship.

#### **Supplementary Material**

All data are publicly available as supporting information to this document.

Table 1. Summary of (semi-)quantitative BWO proxies.

Proxy	Required	BWO	Proxy uncertainties and limitations	Original
	materials	sensitivity		references
$\Delta\delta^{13}C$	Cibicidoides	20 - 235	Calibration uncertainty of $\pm 17$	McCorkle and
	spp. ( <i>C</i> .	μmol/kg	μmol/kg. Proxy reflects maximum	Emerson
	wuellerstorfi		BWO estimates due to impact of	(1988);
	preferred) and		anaerobic processes in $\delta^{13}C_{Globobulimina}$	Hoogakker et
	Globobulimina		(Jacobel et al., 2020); Limited	al., (2015,
	spp.		appearance of Globobulimina spp. in	2018)
			high productivity area (Jorissen et al.,	
			2007); over-estimates BWO in low-	
			BWO sites (this study).	
C <sub>37</sub> alkenone	Bulk sediments	<~50	Reflects maximum BWO estimates;	Anderson et al.
concentrations		μmol/kg	modern calibration only from Arabian	(2019)
			Sea; no straightforward relationship	
			between alkenone spatial abundance	
			and BWO on a global scale, potential	
			dominant impact from export	
			production (Raja and Rosell-Melé,	
			2021).	
Benthic I/Ca	Cibicidoides	<~50	No linear correlation with BWO on	Glock et al.
	spp. or	μmol/kg	global or regional scale; not directly	(2014); Lu et
	Planulina sp.		correlated to in situ oxygen	al. (2020b)
			concentrations; large uncertainties in	
			high BWO; impacted by temperature,	
			salinity, and/or carbonate ion	
			concentration in high BWO conditions	
			(this study).	
Benthic surface	Cibicidoides	<~100	Surface pores are generally only found	Rathburn et al.
porosity	spp. or	μmol/kg	in samples from low-BWO waters; not	(2018)
	Planulina sp.		applicable in high-BWO conditions;	
			calibration uncertainty ~10 μmol/kg at	
			low BWO ranges (this study).	
Benthic	Benthic	<~100	Calibration uncertainty of 10-20	Erdem et al.
assemblages or	foraminifera or	μmol/kg	μmol/kg at Peruvian margin (Erdem et	(2020); Tetard
Eubuliminella	Eubuliminella		al., 2020) or $\pm$ 23-40% of the estimated	et al. (2021a,
tenuata	tenuata		BWO value (Tetard et al., 2021a, b);	b), and
abundance			BWO estimates may be biased to lower	reference
			values or lead to negative values.	therein

Table 2. Radiocarbon dates in TN041-8PG/8JPC

				14C ages		Calibrated	2 sigma (BP
LabID	Core	Depth (cm)	Material	(BP yrs)	Age error	age (BP yrs)	yrs)
OS-162258	TN041-8PG	0.5	G. ruber	885	25	250	52-442
OS-162259	TN041-8PG	112.5	G. ruber	10350	35	11225	10997-11503
OS-162260	TN041-8PG	128.5	G. ruber	11000	35	12208	11918-12476
OS-162397	TN041-8PG	224.5	G. ruber	13650	75	15501	15176-15832
OS-163475	TN041-8JPC	16.5	G. ruber	15250	80	17534	17183-17886
OS-163476	TN041-8JPC	182.5	G. ruber	34600	880	38469	36433-40299
OS-163477	TN041-8JPC	278.5	G. ruber	43900	2700	46053	41685-52199

# **Figures**

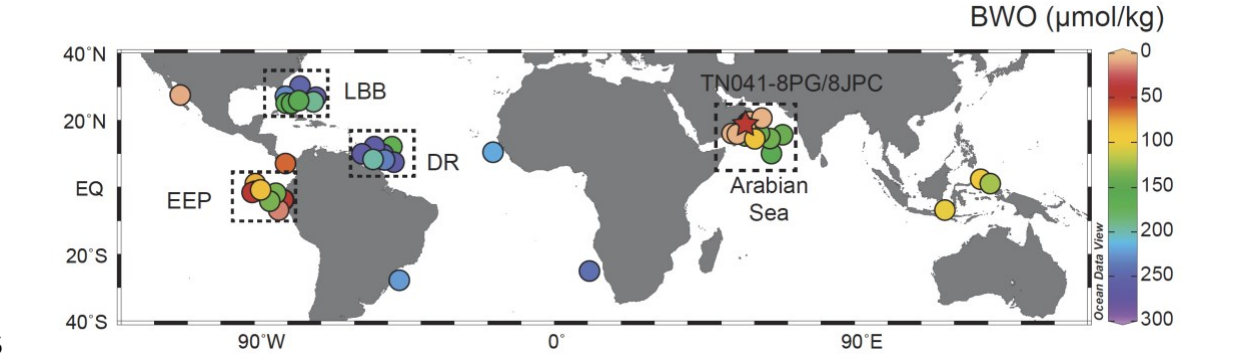


Fig. 1. Sampling locations. Four regional transects are marked with dashed boxes (LBB: Little Bahama Bank; DR: Demerara Rise; EEP: Eastern Equatorial Pacific; and Arabian Sea). Location of sediment cores TN041-8PG/8JPC is marked with a star. Sites are colored by modern BWO based on WOA2018 (Garcia et al., 2019). Figure was generated using Ocean Data View (<a href="https://odv.awi.de/">https://odv.awi.de/</a>) (Schlitzer, 2021).

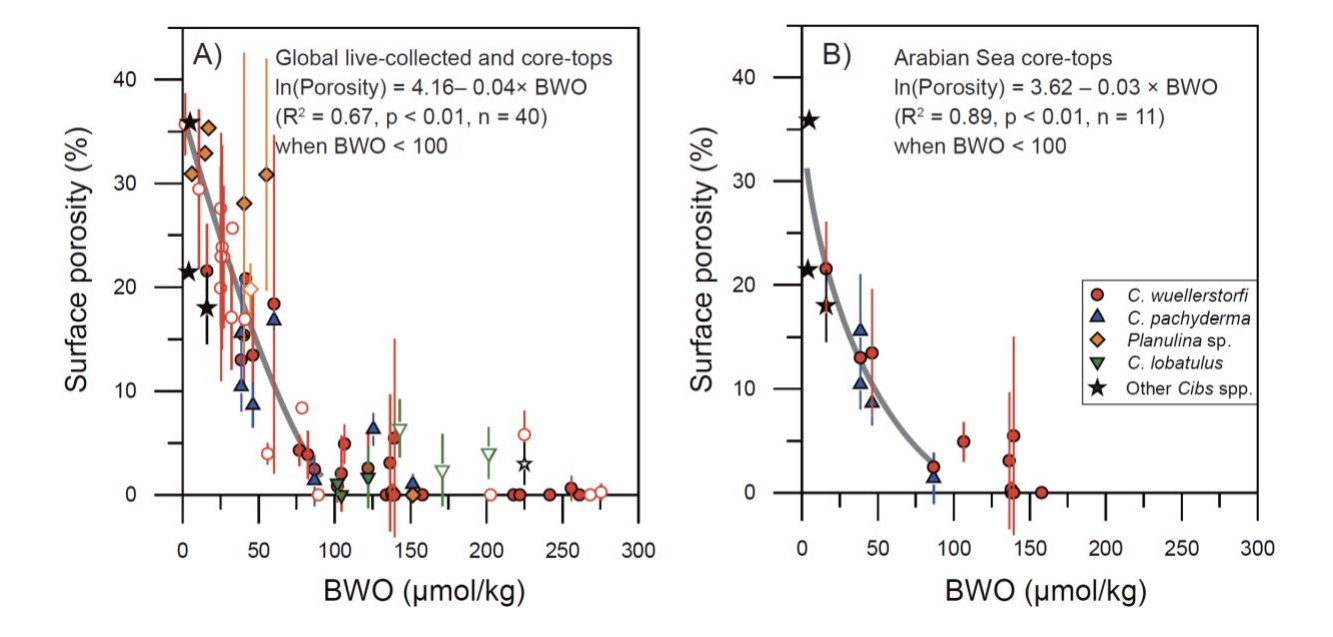


Fig. 2. Benthic foraminiferal surface porosity vs. BWO in globally distributed (A) and Arabian Sea (B) core-top samples. Filled symbols denote samples from this study, whereas open symbols show live-collected samples from a previous study (Rathburn et al., 2018). No systematic offsets were found between different species.

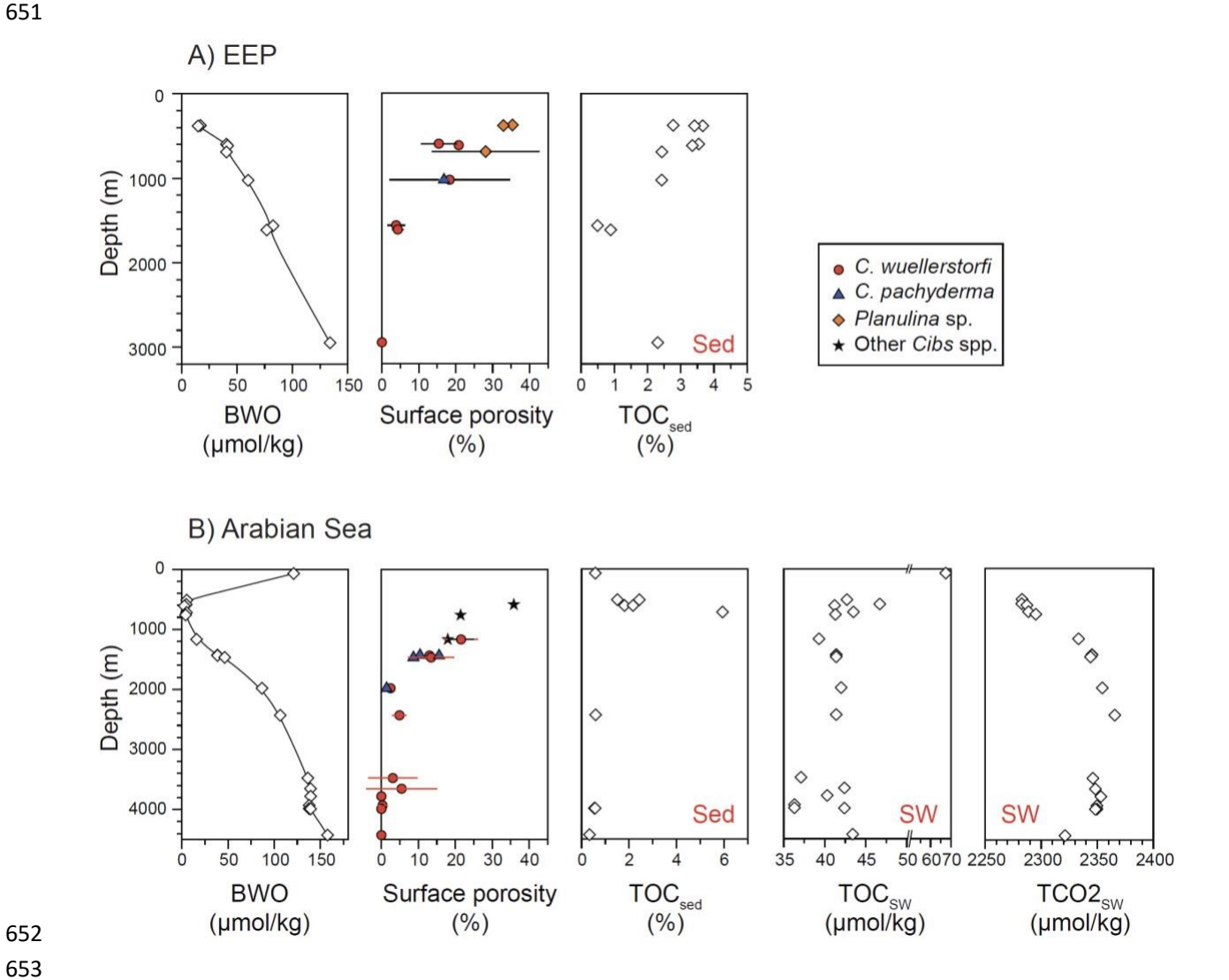


Fig. 3. Depth profiles of BWO, benthic surface porosity, TOCsed from EEP (A) and Arabian Sea (B). The BWO, seawater TOC, and TCO2 profiles in Arabian Sea are extracted from JGOFS database (see Section 3.6 for details). Foraminiferal surface porosity shows an inverse profile to BWO at both locations, with maximum values occurring in the shallowest subsurface samples where BWO is lowest. The TOCsed, TOCsw, or TCO2sw do not show similar profiles with benthic surface porosity.

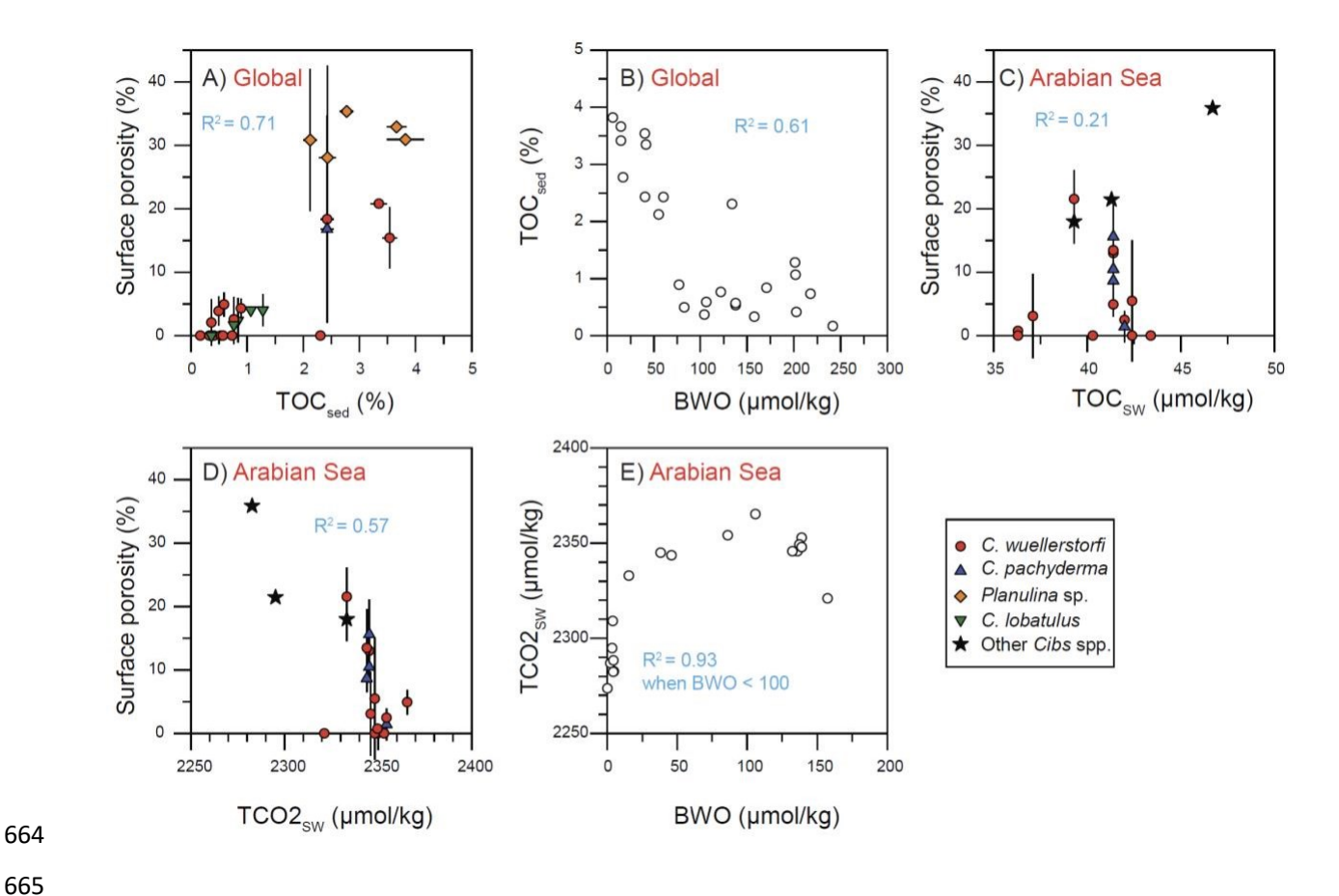


Fig. 4. Relationships between benthic surface porosity, TOC<sub>sed</sub>, BWO, TOC<sub>sw</sub>, and TCO2<sub>sw</sub>. Benthic surface porosity is generally correlated with TOC<sub>sed</sub> due to a correlation between TOC<sub>sed</sub> and BWO. No direct relationships are found between benthic surface porosity and seawater TOC or TCO2 in Arabian Sea.

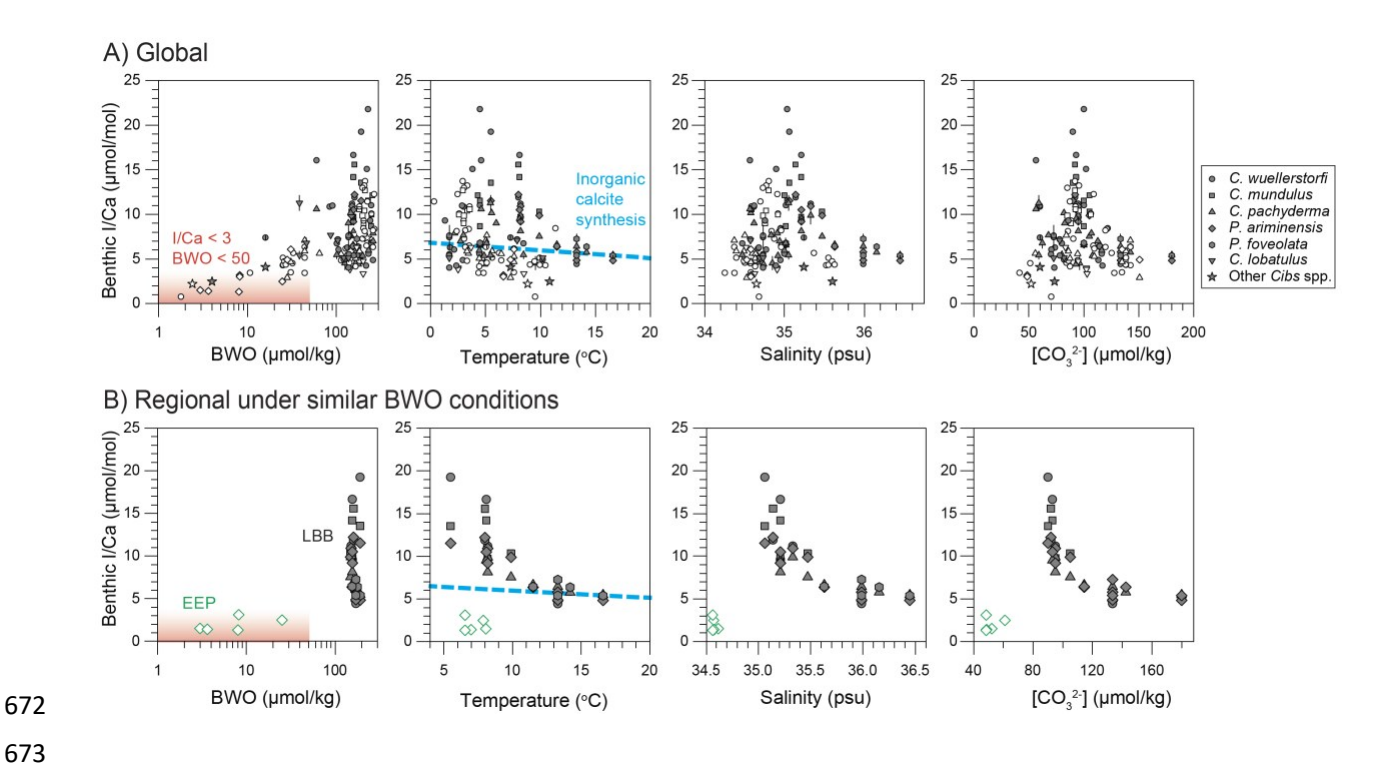


Fig. 5. Cross-plots of benthic I/Ca and hydrographic parameters in the global dataset (A) and data from regional transects (B) within a small BWO range (150-200 μmol/kg in the LBB transect; 0-50 μmol/kg in the EEP transect). Filled symbols denote data from this study, open symbols denote published data in both panels (Glock et al., 2014; Lu et al., 2020). The blue dashed line denotes the temperature vs. I/Ca relationship when [IO<sub>3</sub>-] concentration in solution is 500 nM (equivalent to [IO<sub>3</sub>-] concentrations in oxic seawaters), derived from inorganic calcite synthesis experiments in the laboratory (Zhou et al., 2014). Note that the BWO axis is on a logarithmic scale. The global relationship between I/Ca and BWO is more robust than the relationship with other hydrographic variables. Temperature, salinity, [CO<sub>3</sub><sup>2</sup>-] appear to anti-correlate with I/Ca in high-BWO LBB region, data from the low-BWO EEP region is not consistent with this relationship.

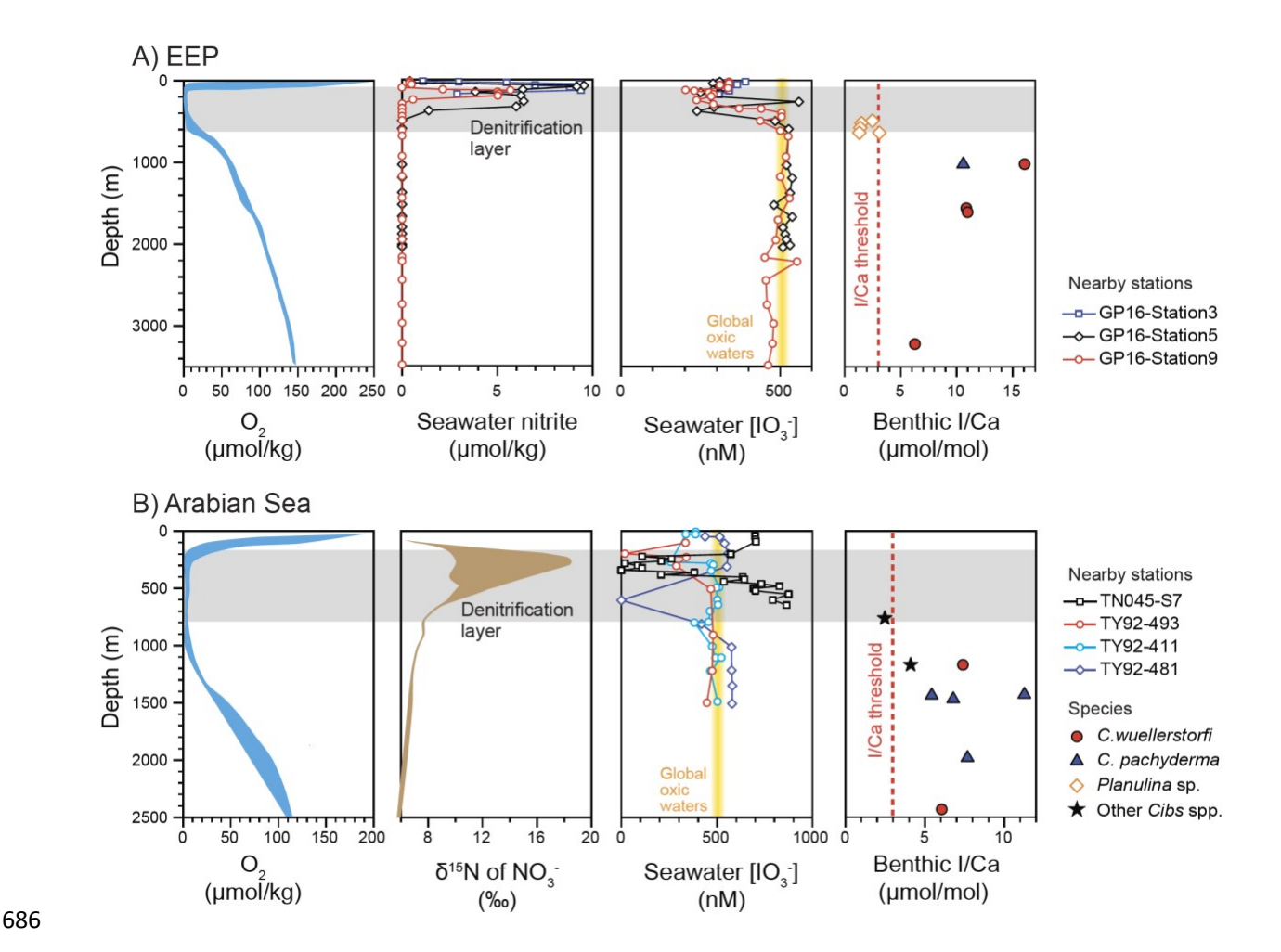


Fig. 6. Depth profiles of oxygen, seawater nitrate (Cutter et al., 2018),  $\delta^{15}N$  range of seawater nitrate (Brandes et al., 1998; Altabet et al., 1999), seawater iodate from nearby stations (Farrenkopf et al., 1997; Farrenkopf and Luther, 2002; Cutter et al., 2018), and benthic I/Ca in EEP (A) and Arabian Sea (B). The yellow shading denotes typical iodate concentrations in global oxic waters (Chance et al., 2014). For stations TY92-411 and TY92-493, the iodate concentrations were calculated from the difference between observed total iodine and iodide; for stations TY92-481 and TN045-S7, the total iodine concentrations were not measured, and we assumed that the maximum concentration of iodide in the water column equals the total iodine and it remains constant throughout the water column, based on observations in northern stations of TN045 cruises (Farrenkopf and Luther, 2002). The grey shading denotes the denitrification layer with oxygen < 10  $\mu$ mol/kg. Low I/Ca < 3  $\mu$ mol/mol appears to track iodate reduction within the denitrification layer in both EEP and Arabian Sea. Note that iodate reduction does not always occur in the denitrification layer.

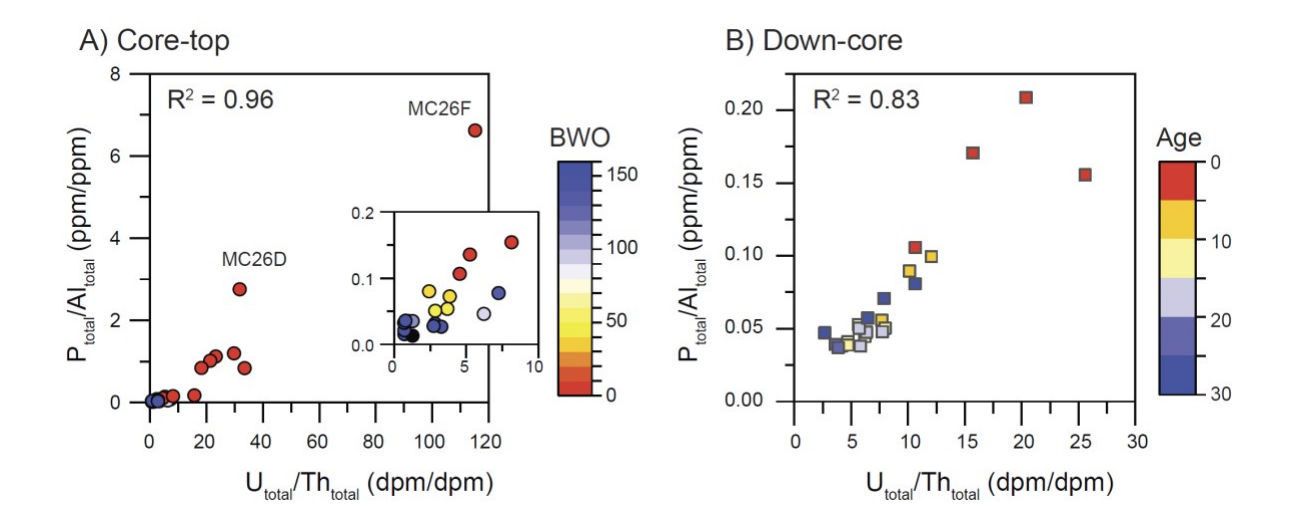


Fig. 7. Cross-plot of Utotal/Thtotal vs. Ptotal/Altotal in the Arabian Sea core-top samples (A) and down-core record (B). Symbols are color coded to highlight OMZ samples in core-top dataset (red and yellow in A) and glacial samples in the down-core record (blue in B). Two core-top sites MC26D and MC26F (see their locations in Fig. S6) show remarkably high U and P contents. The correlations between P/Al and U/Th suggest a close relationship between sedimentary P and U dynamics in Arabian Sea.

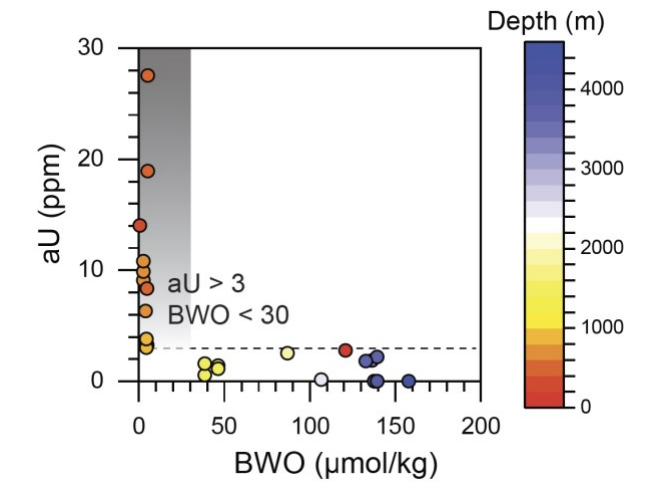


Fig. 8. aU vs. BWO in the Arabian Sea. The aU values were calculated after correcting for lithogenic and apatite components. The OMZ samples in Arabian Sea are only associated with high aU. Statistical results suggest that to identify BWO < 30  $\mu$ mol/kg, the aU threshold is > 3 ppm for Arabian Sea.

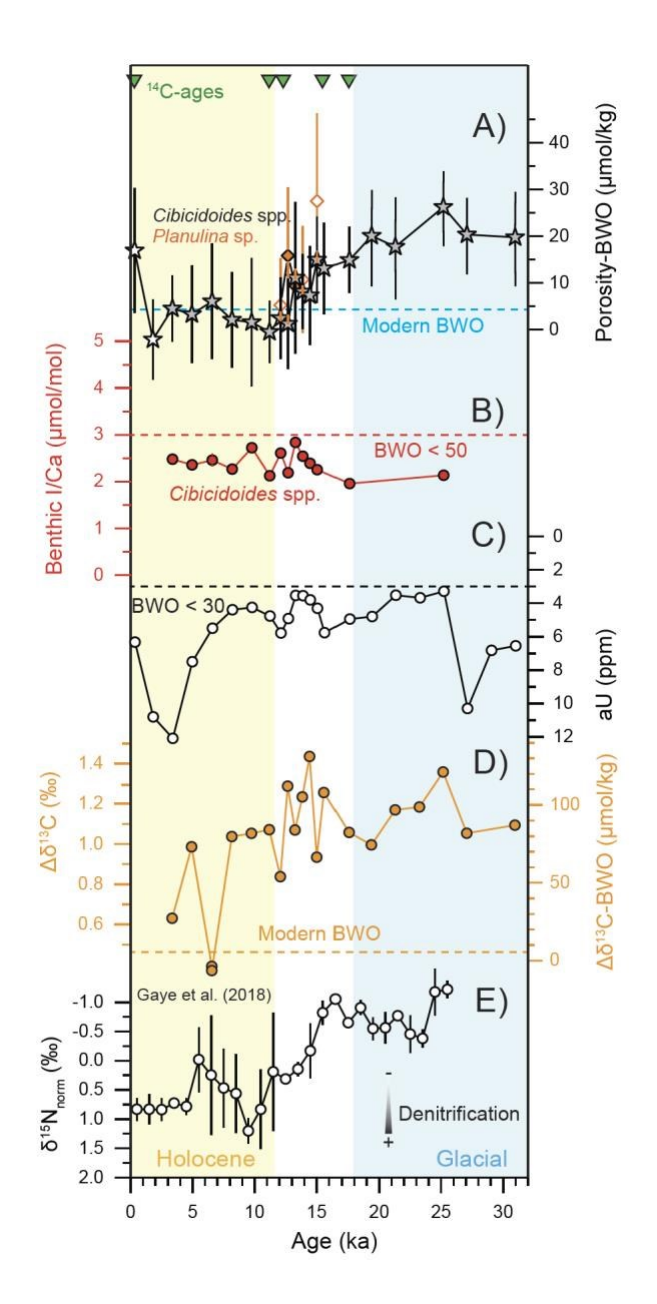


Fig. 9. (A-D) Multi-proxy records of benthic surface porosity, I/Ca, aU, and  $\Delta\delta^{13}C$  versus age for the combined records from TN041-8PG/8JPC. Raw benthic surface porosity and  $\delta^{13}C$  data are presented in Fig. S4. (E) The  $\delta^{15}N$  record represents the regional normalized average of five cores in Oman Margin (Gaye et al. 2018). Large open symbols in the porosity panel denote only one specimen was found in the sample. The benthic surface porosity, I/Ca and aU proxies consistently suggest that BWO was persistently < 50  $\mu$ mol/kg for the past 30 kyr, while the  $\Delta\delta^{13}C$  proxy overestimates the BWO. The porosity, aU, and  $\delta^{15}N$  proxies all suggest higher BWO in the glacial than the Holocene.

#### References

743.

- Altabet M. A., Higginson M. J. and Murray D. W. (2002) The effect of millennial-scale changes in Arabian Sea denitrification on atmospheric CO2. *Nature* **415**, 159-162.
  - Altabet M. A., Murray D. W. and Prell W. L. (1999) Climatically linked oscillations in Arabian Sea denitrification over the past 1 m.y.: Implications for the marine N cycle. *Paleoceanography* **14,** 732-736
- Anderson R. F. (1982) Concentration, vertical flux, and remineralization of particulate uranium in seawater. *Geochim. Cosmochim. Acta* **46**, 1293-1299.
  - Anderson R. F., Fleisher M. Q. and LeHuray A. P. (1989) Concentration, oxidation state, and particulate flux of uranium in the Black Sea. *Geochim. Cosmochim. Acta* **53**, 2215-2224.
  - Anderson R. F., Sachs J. P., Fleisher M. Q., Allen K. A., Yu J., Koutavas A. and Jaccard S. L. (2019) Deep-Sea Oxygen Depletion and Ocean Carbon Sequestration During the Last Ice Age. *Global. Biogeochem. Cy.* **33**, 301-317.
  - Anderson, L.A. and Sarmiento, J.L. (1994). Redfield ratios of remineralization determined by nutrient data analysis. *Global. Biogeochem. Cy.***8**, 65-80.
  - Barker S., Greaves M. and Elderfield H. (2003) A study of cleaning procedures used for foraminiferal Mg/Ca paleothermometry. *Geochem. Geophy. Geosy.* **4**, 8407-8427.
  - Baturin, G.N. and Kochenov, A.V. (2001). Uranium in phosphorites. Lithol. Miner. Resour. 36, 353-373.
  - Beaulieu S. E., Baker E. T., German C. R. and Maffei A. (2013) An authoritative global database for active submarine hydrothermal vent fields. *Geochem. Geophy. Geosy.* **14**, 4892–4905.
  - Bernhard J. M. (1986) Characteristic assemblages and morphologies of benthic foraminifera from anoxic, organic-rich deposits: Jurassic through Holocene. *J. Foramin. Res.* **16**, 207-215.
  - Blaauw M. and Christen J. A. (2011) Flexible paleoclimate age-depth models using an autoregressive gamma process. *Bayesian Anal.* **6**, 457-474.
  - Bradtmiller L. I., Anderson R. F., Sachs J. P. and Fleisher M. Q. (2010) A deeper respired carbon pool in the glacial equatorial Pacific Ocean. *Earth Planet. Sc. Lett.* **299**, 417-425.
  - Brandes J. A., Devol A. H., Yoshinari T., Jayakumar D. A. and Naqvi S. W. A. (1998) Isotopic composition of nitrate in the central Arabian Sea and eastern tropical North Pacific: A tracer for mixing and nitrogen cycles. *Limnol. Oceanogr.* **43**, 1680-1689.
  - Canfield D. E. (1994) Factors influencing organic carbon preservation in marine sediments. *Chem. Geol.* **114**, 315-329.
  - Chance R., Baker A. R., Carpenter L. and Jickells T. D. (2014) The distribution of iodide at the sea surface. *Environ. Sci.-Proc. Imp.* **16**, 1841-1859.
  - Cliff E., Khatiwala S. and Schmittner A. (2021) Glacial deep ocean deoxygenation driven by biologically mediated air—sea disequilibrium. *Nat. Geosci.* **14**, 43-50.
  - Cline J. D. and Kaplan I. R. (1975) Isotopic fractionation of dissolved nitrate during denitrification in the eastern tropical north pacific ocean. *Mar. Chem.* **3,** 271-299.
  - Costa K. M., Anderson R. F., McManus J. F., Winckler G., Middleton J. L. and Langmuir C. H. (2018) Trace element (Mn, Zn, Ni, V) and authigenic uranium (aU) geochemistry reveal sedimentary redox history on the Juan de Fuca Ridge, North Pacific Ocean. *Geochim. Cosmochim. Acta* **236**, 79-98.
- 771 Costa K. M., Hayes C. T., Anderson R. F., Pavia F. J., Bausch A., Deng F., Dutay J. C., Geibert W., Heinze C.,

- Henderson G., Hillaire-Marcel C., Hoffmann S., Jaccard S. L., Jacobel A. W., Kienast S. S., Kipp L.,
  Lerner P., Lippold J., Lund D., Marcantonio F., McGee D., McManus J. F., Mekik F., Middleton J. L.,
  Missiaen L., Not C., Pichat S., Robinson L. F., Rowland G. H., Roy-Barman M., Tagliabue A., Torfstein
  A., Winckler G. and Zhou Y. (2020) 230Th Normalization: New Insights on an Essential Tool for
  Quantifying Sedimentary Fluxes in the Modern and Quaternary Ocean. *Paleoceanogr. Paleoclimatol.*35, e2019PA003820.

  Cutter G.A. Moffett J.W. Nielsdóttir M.C. and Sanial V. (2018) Multiple oxidation state trace elements
- 778 Cutter, G.A., Moffett, J.W., Nielsdóttir, M.C. and Sanial, V. (2018) Multiple oxidation state trace elements 779 in suboxic waters off Peru: In situ redox processes and advective/diffusive horizontal transport. *Mar.* 780 *Chem.* **201**, 77-89.
- Frdem Z., Schönfeld J., Rathburn A. E., Pérez M. E., Cardich J. and Glock N. (2020) Bottom-water deoxygenation at the Peruvian margin during the last deglaciation recorded by benthic foraminifera. 783 *Biogeosciences* **17**, 3165-3182.
- Farrenkopf A. M. and Luther G. W. (2002) Iodine chemistry reflects productivity and denitrification in the
  Arabian Sea: Evidence for flux of dissolved species from sediments of western India into the OMZ. 786

  Deep-Sea Res. Pt. II 49, 2303-2318.
- Farrenkopf A. M., Luther G. W., Truesdale V. W. and van der Weijden C. H. (1997) Sub-surface iodide maxima: Evidence for biologically catalyzed redox cycling in Arabian Sea OMZ during the SW 789 intermonsoon. *Deep-Sea Res. Pt. II* **44**, 1391-1409.
- Feng X. and Redfern S. A. T. (2018) Iodate in calcite, aragonite and vaterite CaCO3: Insights from first-principles calculations and implications for the I/Ca geochemical proxy. *Geochim. Cosmochim. Acta* 792 **236**, 351-360.
- Filippelli G. M. and Delaney M. L. (1996) Phosphorus geochemistry of equatorial Pacific sediments. *Geochim. Cosmochim. Acta* **60,** 1479-1495.
- Fontanier C., MacKensen A., Jorissen F. J., Anschutz P., Licari L. and Griveaud C. (2006) Stable oxygen and carbon isotopes of live benthic foraminifera from the Bay of Biscay: Microhabitat impact and seasonal variability. *Mar. Micropaleontol.* **58**, 159-183.
- Garcia H. E., Weathers K., Paver C. R., Smolyar I., Boyer T. P., Locarnini R. A., Zweng M. M., Mishonov A. v.,
  Baranova O. K., Seidov D. and Reagan J. R. (2019) World Ocean Atlas 2018, Volume 3: Dissolved 800
  Oxygen, Apparent Oxygen Utilization, and Oxygen Saturation. (eds. A. Mishonov) *NOAA Atlas NESDIS* 801
  83, 38pp.
- Gaye B., Böll A., Segschneider J., Burdanowitz N., Emeis K. C., Ramaswamy V., Lahajnar N., Lückge A. and Rixen T. (2018) Glacial-interglacial changes and Holocene variations in Arabian Sea denitrification.

  Biogeosciences 15, 507-527.
- German C. R. and Seyfried W. E. (2013) Hydrothermal Processes. In *Treatise on Geochemistry,* 2nd edition (eds. H. Turekian, H.) Amsterdam: Elsevier, **8**, 191-233.
- Glock N., Eisenhauer A., Milker Y., Liebetrau V., Schönfeld J., Mallon J., Sommer S. and Hensen C. (2011) Environmental influences on the pore density of Bolivina spissa (Cushman). *J. Foramin. Res.* **41**, 22-809

32.

Glock N., Liebetrau V. and Eisenhauer A. (2014) I/Ca ratios in benthic foraminifera from the Peruvian oxygen minimum zone: Analytical methodology and evaluation as a proxy for redox conditions.

Biogeosciences 11, 7077-7095.Glock N., Schönfeld J. and Mallon J. (2012) The Functionality of Pores

813 in Benthic Foraminifera in View of Bottom Water Oxygenation: A Review. In A.V. Altenbach et al. (eds.), Anoxia: Evidence for Eukaryote Survival and Paleontological Strategies, Cellular Origin, Life in 814 Extreme Habitats and Astrobiology 21, 537–552 815 816 Gottschalk J., Vázquez Riveiros N., Waelbroeck C., Skinner L. C., Michel E., Duplessy J. C., Hodell D. and 817 Mackensen A. (2016) Carbon isotope offsets between benthic foraminifer species of the genus 818 Cibicides (Cibicidoides) in the glacial sub-Antarctic Atlantic. Paleoceanography 31, 1583-1602. 819 Hansell D. A. and Peltzer E. T. (1998) Spatial and temporal variations of total organic carbon in the Arabian 820 Sea. Deep-Sea Res. Pt. II 45, 2171-2193. 821 Hardisty D. S., Horner T. J., Evans N., Moriyasu R., Babbin A. R., Wankel S. D., Moffett J. W. and Nielsen S. 822 G. (2021) Limited iodate reduction in shipboard seawater incubations from the Eastern Tropical 823 North Pacific oxygen deficient zone. Earth Planet. Sc. Lett. 554, 116676. Heaton T. J., Köhler P., Butzin M., Bard E., Reimer R. W., Austin W. E. N., Bronk Ramsey C., Grootes P. M., 824 825 Hughen K. A., Kromer B., Reimer P. J., Adkins J., Burke A., Cook M. S., Olsen J. and Skinner L. C. (2020) 826 Marine 20 - The Marine Radiocarbon Age Calibration Curve (0-55,000 cal BP). Radiocarbon 62, 779-827 820. 828 Henderson G. M. and Anderson R. F. (2003) The U-series toolbox for paleoceanography. Rev. Mineral. 829 Geochem. **52**, 493-531. Hoogakker B. A. A., Elderfield H., Schmiedl G., McCave I. N. and Rickaby R. E. M. (2015) Glacial-interglacial 830 831 changes in bottom-water oxygen content on the Portuguese margin. Nat. Geosci. 8, 40-43. 832 Hoogakker B. A. A., Lu Z., Umling N., Jones L., Zhou X., Rickaby R. E. M., Thunell R., Cartapanis O. and 833 Galbraith E. (2018) Glacial expansion of oxygen-depleted seawater in the eastern tropical Pacific. 834 *Nature* **562,** 410-413. 835 Jaccard S. L. and Galbraith E. D. (2012) Large climate-driven changes of oceanic oxygen concentrations 836 during the last deglaciation. Nat. Geosci. 5, 151-156. 837 Jaccard S. L., Galbraith E. D., Martínez-Garciá A. and Anderson R. F. (2016) Covariation of deep Southern Ocean oxygenation and atmospheric CO2 through the last ice age. Nature 530, 207-210. 838 839 Jacobel A. W., Anderson R. F., Jaccard S. L., McManus J. F., Pavia F. J. and Winckler G. (2020) Deep Pacific 840 storage of respired carbon during the last ice age: Perspectives from bottom water oxygen 841 reconstructions. Quat. Sci. Rev. 230, 106065. 842 Jacobel A. W., McManus J. F., Anderson R. F. and Winckler G. (2017) Repeated storage of respired carbon 843 in the equatorial Pacific Ocean over the last three glacial cycles. Nat. Commun. 8, 1-9. 844 Jorissen F. J., Fontanier C. and Thomas E. (2007) Chapter Seven Paleoceanographical Proxies Based on 845 Deep-Sea Benthic Foraminiferal Assemblage Characteristics. In Developments in Marine Geology 846 (eds. Hillaire–Marcel C., and De Vernal A.) Elsevier, 1, 263-325. 847 Kaiho K. (1994) Benthic foraminiferal dissolved-oxygen index and dissolved-oxygen levels in the modern 848 ocean. Geology 22, 719-722. Kuhnt, T., Friedrich, O., Schmiedl, G., Milker, Y., Mackensen, A. and Lückge, A. (2013) Relationship between 849 850 pore density in benthic foraminifera and bottom-water oxygen content. Deep-Sea Res. Pt. I 76, 85-851 95. 852 Key R. M., Kozyr A., Sabine C. L., Lee K., Wanninkhof R., Bullister J. L., Feely R. A., Millero F. J., Mordy C. 853 and Peng T. H. (2004) A global ocean carbon climatology: Results from Global Data Analysis Project

854 (GLODAP). Global. Biogeochem Cy. 18, GB4031. 855 Kobayashi, H., Oka, A., Yamamoto, A. and Abe-Ouchi, A. (2021). Glacial carbon cycle changes by Southern 856 Ocean processes with sedimentary amplification. Sci. Adv. 7, eabg7723. 857 Kraal P., Slomp C. P., Reed D. C., Reichart G. J. and Poulton S. W. (2012) Sedimentary phosphorus and iron 858 cycling in and below the oxygen minimum zone of the northern Arabian Sea. Biogeosciences 9, 2603-859 2624. 860 Kuhnt T., Friedrich O., Schmiedl G., Milker Y., Mackensen A. and Lückge A. (2013) Relationship between 861 pore density in benthic foraminifera and bottom-water oxygen content. Deep-Sea Res. Pt. 176, 85-862 95. 863 Kuhnt T., Schiebel R., Schmiedl G., Milker Y., Mackensen A. and Friedrich O. (2014) Automated and manual 864 analyses of the pore density-to-oxygen relationship in Globobulimina Turgida (Bailey). J. Foramin. 865 Res. 44, 5-16. Lu W., Barbosa C. F., Rathburn A. E., Xavier P. da M., Cruz A. P. S., Thomas E., Rickaby R. E. M., Zhang Y. G. 866 867 and Lu Z. (2021) Proxies for paleo-oxygenation: A downcore comparison between benthic 868 foraminiferal surface porosity and I/Ca. Palaeogeogr. Palaeoclimatol. Palaeoecol. 579, 110588. 869 Lu W., Dickson A. J., Thomas E., Rickaby R. E. M., Chapman P. and Lu Z. (2020a) Refining the planktic 870 foraminiferal I/Ca proxy: Results from the Southeast Atlantic Ocean. Geochim. Cosmochim. Acta 287, 871 318-327. 872 Lu W., Rickaby R. E. M., Hoogakker B. A. A., Rathburn A. E., Burkett A. M., Dickson A. J., Martínez-Méndez 873 G., Hillenbrand C. D., Zhou X., Thomas E. and Lu Z. (2020b) I/Ca in epifaunal benthic foraminifera: A 874 semi-quantitative proxy for bottom water oxygen in a multi-proxy compilation for glacial ocean 875 deoxygenation. Earth Planet. Sc. Lett. 533, 116055. 876 Lu Z., Jenkyns H. C. and Rickaby R. E. M. (2010) Iodine to calcium ratios in marine carbonate as a paleo-877 redox proxy during oceanic anoxic events. Geology 38, 1107-1110. McCorkle D. C., Corliss B. H. and Farnham C. A. (1997) Vertical distributions and stable isotopic 878 879 compositions of live (stained) benthic foraminifera from the North Carolina and California 880 continental margins. Deep-Sea Res. Pt. I 44, 983-1024. 881 McCorkle D. C. and Emerson S. R. (1988) The relationship between pore water carbon isotopic 882 composition and bottom water oxygen concentration. Geochim. Cosmochim. Acta 52, 1169-1178. 883 Moffitt, S.E., Moffitt, R.A., Sauthoff, W., Davis, C.V., Hewett, K. and Hill, T.M., 2015. Paleoceanographic 884 insights on recent oxygen minimum zone expansion: Lessons for modern oceanography. PloS one, 885 10(1), p.e0115246. Morford J. L. and Emerson S. (1999) The geochemistry of redox sensitive trace metals in sediments. 886 887 Geochim. Cosmochim. Acta 63, 1735-1750. 888 Moriyasu R., Evans N., Bolster K. M., Hardisty D. S. and Moffett J. W. (2020) The Distribution and Redox 889 Speciation of Iodine in the Eastern Tropical North Pacific Ocean. Global. Biogeochem. Cy. 34, 890 e2019GB006302. 891 Morrison J. M., Codispoti L. A., Smith S. L., Wishner K., Flagg C., Gardner W. D., Gaurin S., Naqvi S. W. A., 892 Manghnani V., Prosperie L. and Gundersen J. S. (1999) The oxygen minimum zone in the Arabian Sea 893 during 1995. Deep-Sea Res. Pt. II46, 1903-1931. 894 Naqvi S. W. A. (1987) Some aspects of the oxygen-deficient conditions and denitrification in the Arabian

895	Sea. J. Mar. Res. 45, 1049-1072.
896	Passier H. F., Luther G. W. and de Lange G. J. (1997) Early diagenesis and sulphur speciation in sediments
897	of the Oman Margin, northwestern Arabian Sea. Deep-Sea Res. Pt. II 44, 1361-1380.
898	Pelletier G., Lewis E. and Wallace D. (2005) A calculator for the CO2 system in seawater for Microsoft
899	Excel/VBA. Washington State Department of Ecology, Olympia.
900	Petersen J., Riedel B., Barras C., Pays O., Guihéneuf A., Mabilleau G., Schweizer M., Meysman F. J. R. and
901	Jorissen F. J. (2016) Improved methodology for measuring pore patterns in the benthic foraminiferal
902	genus Ammonia. Mar. Micropaleontol. 128, 1-13.
903	Piña-Ochoa E., Høgslund S., Geslin E., Cedhagen T., Revsbech N. P., Nielsen L. P., Schweizer M., Jorissen F.,
904	Rysgaard S. and Risgaard-Petersen N. (2010) Widespread occurrence of nitrate storage and
905	denitrification among Foraminifera and Gromiida. P. Natl. Acad. Sci. USA 107, 1148-1153.
906	Podder J., Lin J., Sun W., Botis S. M., Tse J., Chen N., Hu Y., Li D., Seaman J. and Pan Y. (2017) lodate in 907
calcite and	I vaterite: Insights from synchrotron X-ray absorption spectroscopy and first-principles 908
calculations	. Geochim. Cosmochim. Acta <b>198,</b> 218-228.
909	Raja M. and Rosell-Melé A. (2021) Appraisal of sedimentary alkenones for the quantitative reconstruction
910	of phytoplankton biomass. P. Natl. Acad. Sci. USA 118, e2014787118.
911	Rathburn A. E., Willingham J., Ziebis W., Burkett A. M. and Corliss B. H. (2018) A New biological proxy for
912	deep-sea paleo-oxygen: Pores of epifaunal benthic foraminifera. Sci. Rep. 8, 1-8.
913	Resing J. A., Sedwick P. N., German C. R., Jenkins W. J., Moffett J. W., Sohst B. M. and Tagliabue A. (2015)
914	Basin-scale transport of hydrothermal dissolved metals across the South Pacific Ocean. Nature 523, 915
200-203.	
200-203. 916	Rosenthal Y., Lear C. H., Oppo D. W. and Linsley B. K. (2006) Temperature and carbonate ion effects on
	Rosenthal Y., Lear C. H., Oppo D. W. and Linsley B. K. (2006) Temperature and carbonate ion effects on Mg/Ca and Sr/Ca ratios in benthic foraminifera: Aragonitic species Hoeglundina elegans. 918
916 917	
916 917	Mg/Ca and Sr/Ca ratios in benthic foraminifera: Aragonitic species Hoeglundina elegans. 918
916 917 Paleoceanog	Mg/Ca and Sr/Ca ratios in benthic foraminifera: Aragonitic species Hoeglundina elegans. 918 graphy 21, PA1007.
916 917 <i>Paleoceanog</i> 919	Mg/Ca and Sr/Ca ratios in benthic foraminifera: Aragonitic species Hoeglundina elegans. 918 graphy <b>21</b> , PA1007.  Rudnick, R.L. and Gao, S. (2003) Composition of the continental crust. In: Rudnick, R.L., Holland, H.D.,
916 917 <i>Paleoceanog</i> 919 920	Mg/Ca and Sr/Ca ratios in benthic foraminifera: Aragonitic species Hoeglundina elegans. 918 graphy 21, PA1007.  Rudnick, R.L. and Gao, S. (2003) Composition of the continental crust. In: Rudnick, R.L., Holland, H.D., Turekian, K.K. (Eds.), <i>Treatise of Geochemistry</i> . Elsevier, 1–64.  Rue E. L., Smith G. J., Cutter G. A. and Bruland K. W. (1997) The response of trace element redox couples to suboxic conditions in the water column. <i>Deep-Sea Res. Pt. I44</i> , 113-134.
916 917 <i>Paleoceanog</i> 919 920 921	Mg/Ca and Sr/Ca ratios in benthic foraminifera: Aragonitic species Hoeglundina elegans. 918 graphy 21, PA1007.  Rudnick, R.L. and Gao, S. (2003) Composition of the continental crust. In: Rudnick, R.L., Holland, H.D., Turekian, K.K. (Eds.), <i>Treatise of Geochemistry</i> . Elsevier, 1–64.  Rue E. L., Smith G. J., Cutter G. A. and Bruland K. W. (1997) The response of trace element redox couples
916 917 Paleoceanog 919 920 921 922	Mg/Ca and Sr/Ca ratios in benthic foraminifera: Aragonitic species Hoeglundina elegans. 918 graphy 21, PA1007.  Rudnick, R.L. and Gao, S. (2003) Composition of the continental crust. In: Rudnick, R.L., Holland, H.D., Turekian, K.K. (Eds.), <i>Treatise of Geochemistry</i> . Elsevier, 1–64.  Rue E. L., Smith G. J., Cutter G. A. and Bruland K. W. (1997) The response of trace element redox couples to suboxic conditions in the water column. <i>Deep-Sea Res. Pt. I44</i> , 113-134.
916 917 <i>Paleoceanog</i> 919 920 921 922 923	Mg/Ca and Sr/Ca ratios in benthic foraminifera: Aragonitic species Hoeglundina elegans. 918 graphy 21, PA1007.  Rudnick, R.L. and Gao, S. (2003) Composition of the continental crust. In: Rudnick, R.L., Holland, H.D., Turekian, K.K. (Eds.), <i>Treatise of Geochemistry</i> . Elsevier, 1–64.  Rue E. L., Smith G. J., Cutter G. A. and Bruland K. W. (1997) The response of trace element redox couples to suboxic conditions in the water column. <i>Deep-Sea Res. Pt. I44</i> , 113-134.  Schenau S. J., Reichart G. J. and de Lange G. J. (2005) Phosphorus burial as a function of paleoproductivity
916 917 Paleoceanog 919 920 921 922 923 924 925 926	<ul> <li>Mg/Ca and Sr/Ca ratios in benthic foraminifera: Aragonitic species Hoeglundina elegans. 918 graphy 21, PA1007.</li> <li>Rudnick, R.L. and Gao, S. (2003) Composition of the continental crust. In: Rudnick, R.L., Holland, H.D., Turekian, K.K. (Eds.), <i>Treatise of Geochemistry</i>. Elsevier, 1–64.</li> <li>Rue E. L., Smith G. J., Cutter G. A. and Bruland K. W. (1997) The response of trace element redox couples to suboxic conditions in the water column. <i>Deep-Sea Res. Pt. I44</i>, 113-134.</li> <li>Schenau S. J., Reichart G. J. and de Lange G. J. (2005) Phosphorus burial as a function of paleoproductivity and redox conditions in Arabian Sea sediments. <i>Geochim. Cosmochim. Acta</i> 69, 919-931.</li> <li>Schenau S. J., Slomp C. P. and de Lange G. J. (2000) Phosphogenesis and active phosphorite formation in sediments from the Arabian Sea oxygen minimum zone. <i>Mar. Geol.</i> 169, 1-20.</li> </ul>
916 917 Paleoceanog 919 920 921 922 923 924 925 926 927	<ul> <li>Mg/Ca and Sr/Ca ratios in benthic foraminifera: Aragonitic species Hoeglundina elegans. 918 graphy 21, PA1007.</li> <li>Rudnick, R.L. and Gao, S. (2003) Composition of the continental crust. In: Rudnick, R.L., Holland, H.D., Turekian, K.K. (Eds.), <i>Treatise of Geochemistry</i>. Elsevier, 1–64.</li> <li>Rue E. L., Smith G. J., Cutter G. A. and Bruland K. W. (1997) The response of trace element redox couples to suboxic conditions in the water column. <i>Deep-Sea Res. Pt. I44</i>, 113-134.</li> <li>Schenau S. J., Reichart G. J. and de Lange G. J. (2005) Phosphorus burial as a function of paleoproductivity and redox conditions in Arabian Sea sediments. <i>Geochim. Cosmochim. Acta</i> 69, 919-931.</li> <li>Schenau S. J., Slomp C. P. and de Lange G. J. (2000) Phosphogenesis and active phosphorite formation in sediments from the Arabian Sea oxygen minimum zone. <i>Mar. Geol.</i> 169, 1-20.</li> <li>Schlitzer R. (2021) Ocean Data View, https://odv.awi.de/.</li> </ul>
916 917 Paleoceanog 919 920 921 922 923 924 925 926 927 928	<ul> <li>Mg/Ca and Sr/Ca ratios in benthic foraminifera: Aragonitic species Hoeglundina elegans. 918 graphy 21, PA1007.</li> <li>Rudnick, R.L. and Gao, S. (2003) Composition of the continental crust. In: Rudnick, R.L., Holland, H.D., Turekian, K.K. (Eds.), <i>Treatise of Geochemistry</i>. Elsevier, 1–64.</li> <li>Rue E. L., Smith G. J., Cutter G. A. and Bruland K. W. (1997) The response of trace element redox couples to suboxic conditions in the water column. <i>Deep-Sea Res. Pt. I44</i>, 113-134.</li> <li>Schenau S. J., Reichart G. J. and de Lange G. J. (2005) Phosphorus burial as a function of paleoproductivity and redox conditions in Arabian Sea sediments. <i>Geochim. Cosmochim. Acta</i> 69, 919-931.</li> <li>Schenau S. J., Slomp C. P. and de Lange G. J. (2000) Phosphogenesis and active phosphorite formation in sediments from the Arabian Sea oxygen minimum zone. <i>Mar. Geol.</i> 169, 1-20.</li> <li>Schlitzer R. (2021) Ocean Data View, https://odv.awi.de/.</li> <li>Schoepfer S. D., Shen J., Wei H., Tyson R. v., Ingall E. and Algeo T. J. (2015) Total organic carbon, organic</li> </ul>
916 917 Paleoceanog 919 920 921 922 923 924 925 926 927 928 929	<ul> <li>Mg/Ca and Sr/Ca ratios in benthic foraminifera: Aragonitic species Hoeglundina elegans. 918 graphy 21, PA1007.</li> <li>Rudnick, R.L. and Gao, S. (2003) Composition of the continental crust. In: Rudnick, R.L., Holland, H.D., Turekian, K.K. (Eds.), <i>Treatise of Geochemistry</i>. Elsevier, 1–64.</li> <li>Rue E. L., Smith G. J., Cutter G. A. and Bruland K. W. (1997) The response of trace element redox couples to suboxic conditions in the water column. <i>Deep-Sea Res. Pt. 144</i>, 113-134.</li> <li>Schenau S. J., Reichart G. J. and de Lange G. J. (2005) Phosphorus burial as a function of paleoproductivity and redox conditions in Arabian Sea sediments. <i>Geochim. Cosmochim. Acta</i> 69, 919-931.</li> <li>Schenau S. J., Slomp C. P. and de Lange G. J. (2000) Phosphogenesis and active phosphorite formation in sediments from the Arabian Sea oxygen minimum zone. <i>Mar. Geol.</i> 169, 1-20.</li> <li>Schlitzer R. (2021) Ocean Data View, https://odv.awi.de/.</li> <li>Schoepfer S. D., Shen J., Wei H., Tyson R. v., Ingall E. and Algeo T. J. (2015) Total organic carbon, organic phosphorus, and biogenic barium fluxes as proxies for paleomarine productivity. <i>Earth-Sci. Rev.</i> 149,</li> </ul>
916 917 Paleoceanog 919 920 921 922 923 924 925 926 927 928 929 930	<ul> <li>Mg/Ca and Sr/Ca ratios in benthic foraminifera: Aragonitic species Hoeglundina elegans. 918 graphy 21, PA1007.</li> <li>Rudnick, R.L. and Gao, S. (2003) Composition of the continental crust. In: Rudnick, R.L., Holland, H.D., Turekian, K.K. (Eds.), <i>Treatise of Geochemistry</i>. Elsevier, 1–64.</li> <li>Rue E. L., Smith G. J., Cutter G. A. and Bruland K. W. (1997) The response of trace element redox couples to suboxic conditions in the water column. <i>Deep-Sea Res. Pt. I44</i>, 113-134.</li> <li>Schenau S. J., Reichart G. J. and de Lange G. J. (2005) Phosphorus burial as a function of paleoproductivity and redox conditions in Arabian Sea sediments. <i>Geochim. Cosmochim. Acta</i> 69, 919-931.</li> <li>Schenau S. J., Slomp C. P. and de Lange G. J. (2000) Phosphogenesis and active phosphorite formation in sediments from the Arabian Sea oxygen minimum zone. <i>Mar. Geol.</i> 169, 1-20.</li> <li>Schlitzer R. (2021) Ocean Data View, https://odv.awi.de/.</li> <li>Schoepfer S. D., Shen J., Wei H., Tyson R. v., Ingall E. and Algeo T. J. (2015) Total organic carbon, organic phosphorus, and biogenic barium fluxes as proxies for paleomarine productivity. <i>Earth-Sci. Rev.</i> 149, 23-52.</li> </ul>
916 917 Paleoceanog 919 920 921 922 923 924 925 926 927 928 929 930 931	<ul> <li>Mg/Ca and Sr/Ca ratios in benthic foraminifera: Aragonitic species Hoeglundina elegans. 918 graphy 21, PA1007.</li> <li>Rudnick, R.L. and Gao, S. (2003) Composition of the continental crust. In: Rudnick, R.L., Holland, H.D., Turekian, K.K. (Eds.), <i>Treatise of Geochemistry</i>. Elsevier, 1–64.</li> <li>Rue E. L., Smith G. J., Cutter G. A. and Bruland K. W. (1997) The response of trace element redox couples to suboxic conditions in the water column. <i>Deep-Sea Res. Pt. I44</i>, 113-134.</li> <li>Schenau S. J., Reichart G. J. and de Lange G. J. (2005) Phosphorus burial as a function of paleoproductivity and redox conditions in Arabian Sea sediments. <i>Geochim. Cosmochim. Acta</i> 69, 919-931.</li> <li>Schenau S. J., Slomp C. P. and de Lange G. J. (2000) Phosphogenesis and active phosphorite formation in sediments from the Arabian Sea oxygen minimum zone. <i>Mar. Geol.</i> 169, 1-20.</li> <li>Schlitzer R. (2021) Ocean Data View, https://odv.awi.de/.</li> <li>Schoepfer S. D., Shen J., Wei H., Tyson R. v., Ingall E. and Algeo T. J. (2015) Total organic carbon, organic phosphorus, and biogenic barium fluxes as proxies for paleomarine productivity. <i>Earth-Sci. Rev.</i> 149, 23-52.</li> <li>Shankar R., Subbarao K. v. and Reddy G. R. (1987) Distribution and origin of uranium in surficial sediments</li> </ul>
916 917 Paleoceanog 919 920 921 922 923 924 925 926 927 928 929 930 931 932	<ul> <li>Mg/Ca and Sr/Ca ratios in benthic foraminifera: Aragonitic species Hoeglundina elegans. 918 graphy 21, PA1007.</li> <li>Rudnick, R.L. and Gao, S. (2003) Composition of the continental crust. In: Rudnick, R.L., Holland, H.D., Turekian, K.K. (Eds.), <i>Treatise of Geochemistry</i>. Elsevier, 1–64.</li> <li>Rue E. L., Smith G. J., Cutter G. A. and Bruland K. W. (1997) The response of trace element redox couples to suboxic conditions in the water column. <i>Deep-Sea Res. Pt. I44</i>, 113-134.</li> <li>Schenau S. J., Reichart G. J. and de Lange G. J. (2005) Phosphorus burial as a function of paleoproductivity and redox conditions in Arabian Sea sediments. <i>Geochim. Cosmochim. Acta</i> 69, 919-931.</li> <li>Schenau S. J., Slomp C. P. and de Lange G. J. (2000) Phosphogenesis and active phosphorite formation in sediments from the Arabian Sea oxygen minimum zone. <i>Mar. Geol.</i> 169, 1-20.</li> <li>Schlitzer R. (2021) Ocean Data View, https://odv.awi.de/.</li> <li>Schoepfer S. D., Shen J., Wei H., Tyson R. v., Ingall E. and Algeo T. J. (2015) Total organic carbon, organic phosphorus, and biogenic barium fluxes as proxies for paleomarine productivity. <i>Earth-Sci. Rev.</i> 149, 23-52.</li> <li>Shankar R., Subbarao K. v. and Reddy G. R. (1987) Distribution and origin of uranium in surficial sediments from the Arabian Sea. <i>Chem. Geol.</i> 63, 217-223.</li> </ul>
916 917 Paleoceanog 919 920 921 922 923 924 925 926 927 928 929 930 931	<ul> <li>Mg/Ca and Sr/Ca ratios in benthic foraminifera: Aragonitic species Hoeglundina elegans. 918 graphy 21, PA1007.</li> <li>Rudnick, R.L. and Gao, S. (2003) Composition of the continental crust. In: Rudnick, R.L., Holland, H.D., Turekian, K.K. (Eds.), <i>Treatise of Geochemistry</i>. Elsevier, 1–64.</li> <li>Rue E. L., Smith G. J., Cutter G. A. and Bruland K. W. (1997) The response of trace element redox couples to suboxic conditions in the water column. <i>Deep-Sea Res. Pt. I44</i>, 113-134.</li> <li>Schenau S. J., Reichart G. J. and de Lange G. J. (2005) Phosphorus burial as a function of paleoproductivity and redox conditions in Arabian Sea sediments. <i>Geochim. Cosmochim. Acta</i> 69, 919-931.</li> <li>Schenau S. J., Slomp C. P. and de Lange G. J. (2000) Phosphogenesis and active phosphorite formation in sediments from the Arabian Sea oxygen minimum zone. <i>Mar. Geol.</i> 169, 1-20.</li> <li>Schlitzer R. (2021) Ocean Data View, https://odv.awi.de/.</li> <li>Schoepfer S. D., Shen J., Wei H., Tyson R. v., Ingall E. and Algeo T. J. (2015) Total organic carbon, organic phosphorus, and biogenic barium fluxes as proxies for paleomarine productivity. <i>Earth-Sci. Rev.</i> 149, 23-52.</li> <li>Shankar R., Subbarao K. v. and Reddy G. R. (1987) Distribution and origin of uranium in surficial sediments</li> </ul>

303.

936 Stuiver M., Reimer P. J. and Reimer R. W. (2022) CALIB 8.2. http://calib.org. 937 Tetard M., Licari L., Ovsepyan E., Tachikawa K. and Beaufort L. (2021a) Toward a global calibration for 938 quantifying past oxygenation in oxygen minimum zones using benthic Foraminifera. Biogeosciences 939 **18,** 2827-2841. 940 Tetard M., Ovsepyan E. and Licari L. (2021b) Eubuliminella tenuata as a new proxy for quantifying past 941 bottom water oxygenation. Mar. Micropaleontol. 166, 102016. Tsunogai S. and Sase T. (1969) Formation of iodide-iodine in the ocean. Deep-Sea Res. Pt. I 16, 489-496. 942 Tyson R. v. (2001) Sedimentation rate, dilution, preservation and total organic carbon: Some results of a 943 944 modelling study. Org. Geochem. 32, 333-339. 945 Umling, N.E., Oppo, D.W., Chen, P., Yu, J., Liu, Z., Yan, M., Gebbie, G., Lund, D.C., Pietro, K.R., Jin, Z.D. and 946 Huang, K.F. (2019) Atlantic circulation and ice sheet influences on upper South Atlantic 947 temperatures during the last deglaciation. Paleoceanogr. Paleoclimatol. 34, 990-1005. 948 van der Weijden C. H., Jan Reichart G. and Jan Visser H. (1999) Enhanced preservation of organic matter 949 in sediments deposited within the oxygen minimum zone in the northeastern Arabian Sea. Deep-950 Sea Res. Pt. I 46, 807-830. 951 Wong G. T. F. and Brewer P. G. (1977) The marine chemistry of iodine in anoxic basins. Geochim. 952 Cosmochim. Acta 41, 151-159. 953 Wong G. T. F. and Hung C. C. (2001) Speciation of dissolved iodine: Integrating nitrate uptake over time in 954 the oceans. Cont. Shelf Res. 21, 113-128. 955 Yamamoto A., Abe-Ouchi A., Ohgaito R., Ito A. and Oka A. (2019) Glacial CO2 decrease and deep-water 956 deoxygenation by iron fertilization from glaciogenic dust. Clim. Past 15, 981-996. Zhou X., Thomas E., Rickaby R. E. M., Winguth A. M. E. and Lu Z. (2014) I/Ca evidence for upper ocean 957 958 deoxygenation during the PETM. Paleoceanography 29, 964-975. 959 Zou, K. H., O'Malley, A. J., and Mauri, L. (2007). Receiver-operating characteristic analysis for evaluating diagnostic tests and predictive models. Circulation 115, 654-657. 960